

Supernova feedback in numerical simulations of galaxy formation: separating physics from numerics

Matthew C. Smith^{1*}, Debora Sijacki¹, Sijing Shen^{1,2}

¹ *Institute of Astronomy and Kavli Institute for Cosmology, University of Cambridge, Madingley Road, Cambridge CB3 0HA, UK*

² *Institute of Theoretical Astrophysics, University of Oslo, P.O. Box 1029, Blindern, N-0315, Oslo, Norway*

27 April 2018

ABSTRACT

While feedback from massive stars exploding as supernovae (SNe) is thought to be one of the key ingredients regulating galaxy formation, theoretically it is still unclear how the available energy couples to the interstellar medium and how galactic scale outflows are launched. We present a novel implementation of six sub-grid SN feedback schemes in the moving-mesh code AREPO, including injections of thermal and/or kinetic energy, two parametrizations of delayed cooling feedback and a ‘mechanical’ feedback scheme that injects the correct amount of momentum depending on the relevant scale of the SN remnant resolved. All schemes make use of individually time-resolved SN events. Adopting isolated disk galaxy setups at different resolutions, with the highest resolution runs reasonably resolving the Sedov-Taylor phase of the SN, we aim to find a physically motivated scheme with as few tunable parameters as possible. As expected, simple injections of energy overcool at all but the highest resolution. Our delayed cooling schemes result in overstrong feedback, destroying the disk. The mechanical feedback scheme is efficient at suppressing star formation, agrees well with the Kennicutt-Schmidt relation and leads to converged star formation rates and galaxy morphologies with increasing resolution without fine tuning any parameters. However, we find it difficult to produce outflows with high enough mass loading factors at all but the highest resolution, indicating either that we have oversimplified the evolution of unresolved SN remnants, require other stellar feedback processes to be included, require a better star formation prescription or most likely some combination of these issues.

Key words: galaxies: formation, galaxies: evolution, methods: numerical

1 INTRODUCTION

In the Λ CDM model of cosmology, dark matter dominates large scale structure formation. Gas gathers in the potential wells of dark matter halos, where it may radiatively cool and hence form stars. This baryonic matter makes up the visible component of galaxies. This picture alone is not sufficient to reproduce observations. A naive determination of the expected star formation rate (SFR) based on a typical dynamical time yields excessive values. In fact, star formation occurs on much longer timescales of the order of 20 - 100 dynamical times and has an efficiency of only a few percent (see for example Zuckerman & Evans 1974; Williams & McKee 1997; Kennicutt 1998; Evans 1999; Krumholz & Tan 2007; Evans et al. 2009). Thus, some form of feedback process or processes need to be invoked to explain this discrepancy. At high halo masses, this may be provided by an active galactic nucleus (AGN), but at lower masses stellar

feedback dominates, mainly from high mass stars in the form of stellar winds, supernovae (SNe), photoionisation and radiation pressure.

It is worth emphasising that it is not enough merely to halt the conversion of gas to stars as some fraction of the accreted mass must be ejected out of the galaxy. Without strong feedback, the baryon fraction of galaxy models are far in excess of observations (e.g. White & Frenk 1991; Kereš et al. 2009). In addition, the observed circumgalactic medium (CGM) is enriched with metals, requiring baryons to have made it out from sites of star formation embedded within the galaxies themselves (e.g. Aguirre et al. 2001; Pettini et al. 2003; Songaila 2005, 2006; Martin et al. 2010). Such outflows are observed, moving at hundreds of km s^{-1} (see for example the review by Veilleux et al. 2005). Observations suggest that the ratio of mass outflow rate to SFR (i.e. the mass loading factor) must be at least unity or above (see e.g. Bland-Hawthorn et al. 2007; Schroetter et al. 2015). This is borne out by theoretical models (Oppenheimer &

* E-mail: m.c.smith@ast.cam.ac.uk

Davé 2006; Sales et al. 2010; Genel et al. 2012; Shen et al. 2012; Davé et al. 2013; Puchwein & Springel 2013; Vogelsberger et al. 2013; Hopkins et al. 2014; Mitra et al. 2015; Christensen et al. 2016).

While the observational evidence for SFR regularisation and outflow driving is manifest, precisely how these mechanisms operate is as yet unclear. Here numerical hydrodynamic simulations of galaxy formation are useful tools. Unfortunately, the scales on which stellar feedback operates (parsecs and below) are many orders of magnitude below the characteristic scales of galaxies and the surrounding CGM we wish to simulate.

This ideally needed dynamic range is beyond the reach of current state-of-the-art simulations, requiring the representation of the effects of unresolved processes by adopting so-called ‘sub-grid’ schemes. For large scale cosmological simulations, where the interstellar medium (ISM) is poorly resolved, these schemes must rely on dealing with stellar feedback at a high level of abstraction. For example, such approaches may use effective equations of state to approximate the effect of a multiphase ISM pressurised by feedback energy (e.g. Springel & Hernquist 2003; Teyssier et al. 2010). Winds are often added with some predetermined mass loading, either temporarily decoupling outflowing gas from the hydrodynamics, imposing some minimum threshold temperature of the wind ejecta or switching off radiative cooling losses for a given amount of time, to ensure sufficiently strong driving (e.g. Springel & Hernquist 2003; Oppenheimer & Davé 2006; Dalla Vecchia & Schaye 2008; Sales et al. 2010). Such schemes are presently necessary to model large samples of galaxies but lack predictive power on small scales. However, if the target of a simulation is a single galaxy, either in an idealised, isolated setup or in a cosmological ‘zoom-in’, then the higher resolution available enables the adoption of more explicit models of feedback, allowing investigations of how feedback arises on comparatively smaller scales to be carried out.

Nevertheless, even in the individual galaxy simulations the resolution requirements are still severe. In the case of SNe, one of the main obstacles to physically consistent coupling of SN energy to the ISM is the ability to resolve the Sedov-Taylor phase of a SN remnant. The expansion of SN remnants has been well studied and can be broken down into several distinct regimes (Woltjer 1972). The SN explosion ejects material into the ISM with typical kinetic energies of 10^{51} ergs. The SN ejecta expands relatively unhindered into the ISM as long as the mass swept up in the forward shock is smaller than the ejecta mass. Concurrently, the reverse shock heats up the gas inside the remnants, leading to high temperatures and pressures. Radiative losses are negligible so the expansion proceeds adiabatically into the surrounding medium, which marks the Sedov-Taylor phase. During this phase, the momentum of the remnant is boosted by up to an order of magnitude (Taylor 1950; Sedov 1959; Chevalier 1974; Cioffi et al. 1988; Blondin et al. 1998; Kim & Ostriker 2015; Martizzi et al. 2015). Eventually, a thin, dense shell builds up at the shock front and radiative losses become important, triggering the transition from energy conserving to momentum conserving evolution. Because of the large increase in momentum that occurs during the adiabatic expansion, merely injecting energy (whether thermal or kinetic) into the surrounding gas without properly re-

solving the length scales corresponding to the Sedov-Taylor phase results in a severe underestimation of the amount of momentum imparted to the ISM. Kim & Ostriker (2015) found that the minimum requirements for correctly modelling the evolution of SNe in this manner are that the shell forming radius, r_{SF} , is resolved by three resolution elements. For evolution in an inhomogeneous medium, they quantified that $r_{\text{SF}} = 30 \text{ pc } (n/\text{cm}^{-3})^{-0.46}$, meaning that at a density of 100 cm^{-3} (typical mean density for a giant molecular cloud) the resolution requirement is $\sim 1 \text{ pc}$. Failure to meet these requirements when using a simple injection of SN energy will result in ‘overcooling’ as the energy is radiated away before it can do any work.

Many strategies to circumvent this issue exist in the literature. One implicit solution is to inject the energy of several SNe simultaneously resulting in more energetic explosions. Often, this is achieved simply by injecting a star particle’s entire feedback energy budget at once, either instantaneously or after some predetermined delay time. The strength of this effect is therefore tied to the star particle mass. Alternatively, a stochastic feedback approach, such as that proposed in Dalla Vecchia & Schaye (2012), may be adopted, in which SN energy is redistributed in time and space to produce fewer, more energetic events guaranteeing the overcooling problem is avoided. Such schemes conserve the total feedback energy in a globally averaged sense, but lose the connection to individual SN events and are not spatially consistent. If the simulation is of a coarse resolution and the structure of the ISM is not resolvable/of interest, this may be an acceptable compromise.

A different class of approaches involves switching off the radiative cooling of gas that has received feedback energy, enforcing an adiabatic phase, for some length of time (see e.g. Stinson et al. 2006; Governato et al. 2010; Agertz et al. 2011; Teyssier et al. 2013). The length of time by which cooling is delayed is somewhat of a tunable parameter, particularly in simulations with coarse resolution, but physically motivated parameters can be arrived at by analytical arguments (see for example the appendix of Dubois et al. 2015). A downside of ‘delayed cooling’ models is that the radiative cooling of the gas is physically correct, even if the resolution effects responsible for the overcooling phenomena are not. Thus it is possible for gas to occupy unphysical regions of temperature-density phase diagrams when it should have cooled.

In alternative to the ‘delayed cooling’ schemes, it is possible to take account of the momentum boost in the missed adiabatic phase rather than enforcing such a phase. Some schemes skip the Sedov-Taylor phase entirely, putting in a bubble at some fixed radius and adjusting the kinetic energy of the gas inside to match the analytically determined values assuming some mass loading (see e.g. Dubois & Teyssier 2008). Others determine the stage of a remnant’s evolution that can be resolved and boost the momentum by some appropriate factor determined either analytically (e.g. Hopkins et al. 2014; Kimm & Cen 2014) or by making use of fits to high resolution simulations of SN remnant evolution (e.g. Martizzi et al. 2015 as employed in Martizzi et al. 2016). These schemes are often referred to as mechanical feedback. They feature few (if any) explicitly tunable parameters, but rely on assumptions about the structure of the ISM at small scales and how the remnant will interact with it. For exam-

ple, a porous ISM structure caused by turbulence may allow the remnant to propagate preferentially down low density channels (Iffrig & Hennebelle 2015; Kim & Ostriker 2015; Martizzi et al. 2015; Walch & Naab 2015; Li 2015; Haid et al. 2016) though the net effect of this phenomenon is not well constrained and possibly introduces further free parameters into the model.

Of course, SNe are not the only form of stellar feedback. It is possible for photoionisation to break up star forming clouds prior to the first SNe occurring (Vázquez-Semadeni et al. 2010; Walch et al. 2012; Dale et al. 2014; Sales et al. 2014). Winds from massive stars are unable to completely disrupt $10^4 - 10^5 M_\odot$ clouds, but can carve cavities of ~ 10 pc which may enhance subsequent SNe feedback (Dale et al. 2014). Radiation pressure can in principle supply as much momentum as stellar winds (see e.g. Leitherer et al. 1999), though it is difficult to assess the extent to which this can be coupled to the ISM. On the one hand, H II regions created by massive stars will blunt the impact of radiation pressure, rendering the ISM transparent to Lyman-limit photons, but in the presence of dust, multiple scattering of IR photons can boost the momentum input to the ISM by up to a few orders of magnitude (Murray et al. 2010). Using sub-grid models of radiation pressure feedback it has been found that boost factors of $\sim 10 - 100$ are necessary to drive strong outflows (Hopkins et al. 2011, 2012a,b; Agertz et al. 2013; Aumer et al. 2013; Roškar et al. 2014; Agertz & Kravtsov 2015). However, using full radiative hydrodynamics (RHD), Rosdahl et al. (2015) concluded that radiation pressure is unable to drive strong outflows in their simulations, although they are unable to resolve gas at high enough densities to become significantly optically thick to IR photons. Nevertheless, a simple boosting of the IR optical depths resulted in suppressing star formation and smoothing of the disk without generating outflows. In reality, all of these stellar feedback mechanisms will interact in a complex manner. For example, the FIRE project (Hopkins et al. 2014) has produced encouraging results by including multiple stellar feedback processes in sub-grid fashion, creating realistic looking galaxies relative to observations. However, it is clear that before trying to unpick the interaction of different processes and their impact on galaxy formation, it is crucial to understand the numerical consequences of the individual feedback schemes.

To this end, in this work, we carry out a detailed study of various flavours of SN feedback prescriptions commonly found in the literature. We perform simulations of idealised, isolated galaxy models, in the absence of other feedback prescriptions and with a simple star formation law, in order to provide as clean a comparison as possible. The schemes tested are all chosen to work with individually time resolved SN events, providing as direct a link to the locations and timescales of star formation as possible (e.g. we do not consider stochastic feedback such as Dalla Vecchia & Schaye 2012), and are optimised for isolated or cosmological zoom-in simulations (rather than cosmological boxes). We carry out our fiducial simulations of a $10^{10} M_\odot$ system at three resolutions (the highest of which is chosen to largely eliminate the overcooling problem in a simple thermal dump scheme) in order to test convergence properties, trialing six sub-grid feedback schemes. Having presented our main findings with respect to resulting galaxy morphologies, SFRs, and outflow

properties as function of feedback scheme, we briefly examine how these results depend on the mass of the galaxy and simple changes of the star formation prescription.

2 METHODOLOGY

2.1 Basic Code Setup

We make use of the moving-mesh code AREPO (Springel 2010) with our own novel implementation of star formation and SN feedback (described below). AREPO uses a quasi-Lagrangian finite volume technique, solving hydrodynamics on an unstructured mesh determined by a Voronoi tessellation of discrete mesh-generating points. These points move with the local gas velocity (with the addition of minor corrections to allow for cell regularisation). By moving the mesh with the fluid and employing a smoothly varying refinement and derefinement scheme, AREPO is able to keep cell masses constant (to within a factor ~ 2). AREPO benefits from many of the advantages inherent to traditional Lagrangian approaches (e.g. smoothed particle hydrodynamics (SPH)), such as continuously varying resolution with density and Galilean invariance, while retaining advantages of contemporary Eulerian codes (i.e. adaptive mesh refinement (AMR)) such as more accurate resolution of shocks, contact discontinuities and fluid instabilities (Bauer & Springel 2012; Kereš et al. 2012; Sijacki et al. 2012; Torrey et al. 2012; Vogelsberger et al. 2012). We include radiative cooling from both primordial species and metal-lines as presented in Vogelsberger et al. (2013): primordial heating and cooling rates are calculated using cooling, recombination and collisional rates from Cen (1992) and Katz et al. (1996), while lookup tables pre-calculated with the photoionization code CLOUDY are used to obtain the metal cooling rates. Note that in this work we do not include a UV background.

2.2 Non-thermal pressure floor

Failing to sufficiently resolve the Jeans length can result in artificial fragmentation (Truelove et al. 1997). To avoid this we include a non-thermal pressure floor to ensure that the Jeans length is resolved by N_J cells, i.e.

$$P_{\min} = \frac{N_J^2 \Delta x^2 G \rho^2}{\pi \gamma}, \quad (1)$$

where Δx is the cell diameter, ρ is the gas density and $\gamma = 5/3$ is the adiabatic index. In principle, at sufficiently high resolution if feedback is able to entirely prevent gas from entering a phase where it is vulnerable to artificial fragmentation, it may be possible to avoid the use of a pressure floor. This would ideally prevent the risk of suppressing physical fragmentation which may occur when a pressure floor is in place. Alternatively, the star formation prescription adopted could be formulated to ensure that gas is turned into stars before artificial fragmentation occurs. However, as we only include SNe feedback (note that there is a delay of ~ 3 Myr before the first SNe go off) and wish to study the effects of the feedback without a more involved method of modelling star formation (see below), we use a pressure floor to ensure numerically meaningful gas conditions prior to feedback.

Various values for N_J can be found in the literature. We find that the value required varies depending on choice of code, cooling prescriptions, initial conditions, resolution

and included sub-grid physics. The choice is therefore somewhat arbitrary and often ill defined. By performing an array of numerical experiments, we find that $N_J = 8$ is a reasonable choice for $1000 M_\odot$ cell resolution (see Fig. A1 in Appendix A). It should be noted that in the absence of feedback, the choice of N_J has a significant impact on the total stellar mass formed (see Fig. A2). For the purposes of the comparison of feedback implementations in this work, our choice is therefore motivated by our requirements to avoid the opposite extremes of artificial fragmentation or total suppression of star formation by the pressure floor.

Using a fixed value of N_J with different resolutions ensures that the Jeans length is always resolved by the same number of cells. This means that, by design, fragmentation is allowed to occur on smaller scales as simulations move to higher resolutions and the minimum resolvable scale decreases. While under most circumstances this is a desirable behaviour, the resulting lack of convergence in the absence of feedback makes a meaningful study of the resolution dependence of SN feedback schemes impossible. Thus, for this work, we adopt the scaling $N_J = 8(m_{\text{cell}}/1000 M_\odot)^{-1/3}$ such that the pressure floor corresponds to resolving the same length-scale across all resolutions. This results in relatively similar gas morphologies, temperature and density distributions and SFRs in the absence of feedback at all numerical resolutions explored (see Fig. A3 in Appendix A). With this choice of the pressure floor scaling, starting with relatively similar disk properties in different resolution runs we can more readily isolate how feedback operates at different resolutions. A much more detailed discussion of the use of the pressure floor in this work and its effects on the simulations is presented in Appendix A.

2.3 Star formation

In our model, gas is marked as star forming if it is above some density threshold n_{SF} . We then compute a star formation rate for the gas based on a simple Schmidt law, using the almost ubiquitous expression

$$\dot{\rho}_* = \epsilon_{\text{SF}} \frac{\rho}{t_{\text{ff}}}, \quad (2)$$

where ρ is the gas density, ϵ_{SF} is some efficiency and $t_{\text{ff}} = \sqrt{3\pi/32G\rho}$ is the free-fall time. We use a fiducial value of $n_{\text{SF}} = 10 \text{ cm}^{-3}$ and $\epsilon_{\text{SF}} = 1.5\%$ (chosen to match observed efficiencies in dense gas, see e.g. Krumholz & Tan 2007, and references therein). These values are kept the same across all resolutions for our fiducial simulations (they are an appropriate choice for all resolutions explored), with the aim of removing the dependence the choice of star formation law prescription and allowing us to assess the convergence properties of the SNe schemes alone¹. We then use these rates to stochastically convert gas cells to star particles (representing a single stellar population).

2.4 Supernova feedback

Our implementation of SN feedback is directly related to individual star particles and discretely resolves individual SNe in time. This is in contrast to implementations which inject

¹ However, see Section 3.8 where we present results with a higher density threshold value of $n_{\text{SF}} = 100 \text{ cm}^{-3}$ or a higher efficiency of $\epsilon_{\text{SF}} = 15\%$

energy continuously at some rate related to the SFR and to methods in which a fixed quantity of energy per stellar mass is injected, possibly after some delay. Injecting the energy of multiple SNe at once will help avoid the overcooling problem (the radius of the remnant at the end of the Sedov-Taylor phase has a dependence on injected energy as $E^{0.29}$ (Kim & Ostriker 2015)). However, the local evolution of the ISM with time as it evolves prior to the first SNe and as SNe occur sequentially (for example enhancing the strength of subsequent SNe) is non-trivial. Failing to resolve individual SNe in time potentially misses important physics. Therefore, each timestep, for each star particle, we tabulate SN rates, \dot{N}_{SN} , as a function of age and metallicity from STARBURST99 (Leitherer et al. 1999) assuming a Kroupa (2002) IMF. We then draw the number of SNe that occur from a Poisson distribution with a mean $\bar{N}_{\text{SN}} = \dot{N}_{\text{SN}}\Delta t$, where Δt is the timestep. We further impose a timestep limiter for star particles such that $\bar{N}_{\text{SN}} \ll 1$ to ensure that SNe are individually resolved in time.

When a SN occurs, mass, metals, energy and/or momentum (depending on the feedback scheme, see below) are deposited into the gas cell hosting the star particle and its immediate neighbours (i.e. all cells that share a face with the host cell). The various quantities are distributed amongst these cells using a weighting scheme that aims to guarantee an isotropic distribution. This contrasts with the SPH-like (mass, volume etc.) weighting schemes commonly used in Lagrangian codes. Because higher density regions will contain more resolution elements, such a weighting scheme will preferentially inject feedback quantities perpendicular to the local density gradient. In the worst case scenario, we have found that this manifests itself in the unphysical driving of strong feedback ‘rings’ through the plane of a thin disk, similar to those reported in Hopkins et al. (2017); Hopkins et al. (2018) (see our Appendix B for more details). Our weighting scheme is based on the ‘vector weighting’ scheme from Hopkins et al. (2017) (see Hopkins et al. 2018, for a full derivation of the scheme). Essentially, the quantities are weighted both by the solid angle subtended by the adjoining cell face and by projection operators to enforce isotropy. To compute these quantities we use the mesh geometry used in the hydrodynamic calculation. For reasons of numerical simplification we take the centre of the SNe to be the mesh generating point of the cell hosting the star particle, rather than the star particle itself. The effects of this are small, since by definition the star particle is spatially unresolved in the context of the hydrodynamic resolution. Further simplifications to the Hopkins et al. (2017) scheme arise since the Voronoi tessellation guarantees that cell face norms are aligned with the position vector between two mesh generating points and that cell faces lie exactly halfway between the two mesh generating points in that direction. Note that the centre of the cell face is not guaranteed to lie on the line between two mesh generating points. However, we take this as an approximation. Due to the mesh regularisation schemes used in AREPO, we find this to be reasonable.

We first find the cell that contains the star particle, hereafter referred to as the host cell. For each of the neighbour cells (cells that share a face with the host cell), i , we determine the vector weight $\bar{\mathbf{w}}_i$ defined as

$$\bar{\mathbf{w}}_i = \frac{\mathbf{w}_i}{\sum_j |\mathbf{w}_j|} (1 - f_{\text{host}}), \quad (3)$$

where the sum over j is over all neighbour cells including i ,

$$\mathbf{w}_i = \omega_i \sum_{+,-} \sum_{\alpha} (\hat{\mathbf{x}}_i^{\pm})^{\alpha} f_{\pm}^{\alpha}, \quad (4)$$

$$f_{\pm}^{\alpha} = \left\{ \frac{1}{2} \left[1 + \left(\frac{\sum_j \omega_j |\hat{\mathbf{x}}_j^{\mp}|^{\alpha}}{\sum_j \omega_j |\hat{\mathbf{x}}_j^{\pm}|^{\alpha}} \right)^2 \right] \right\}^{1/2}, \quad (5)$$

$$\omega_i = \frac{1}{2} \left(1 - \frac{1}{\sqrt{1 + 4A_i/(\pi |\mathbf{x}_i|^2)}} \right), \quad (6)$$

$$(\hat{\mathbf{x}}_i^+)^{\alpha} = |\mathbf{x}_i|^{-1} \text{MAX}(\mathbf{x}_i^{\alpha}, 0) \Big|_{\alpha=x,y,z}, \quad (7)$$

$$(\hat{\mathbf{x}}_i^-)^{\alpha} = |\mathbf{x}_i|^{-1} \text{MIN}(\mathbf{x}_i^{\alpha}, 0) \Big|_{\alpha=x,y,z}, \quad (8)$$

where f_{host} is the fraction of feedback quantities given to the host cell, A_i is the area of the face between the neighbour and the host cell, \mathbf{x}_i is the position vector between the mesh generating points of the neighbour to the host, the superscript α denotes the component in a given Cartesian direction, x , y or z , while the $+$ and $-$ denote components with either a positive or negative value respectively. Given a total ejecta mass m_{ej} and SN energy E_{SN} , the total momentum to be injected in the rest frame of the star particle is

$$p_{\text{tot}} = \sqrt{2m_{\text{ej}}f_{\text{kin}}E_{\text{SN}}}, \quad (9)$$

where f_{kin} is the fraction of ejecta energy that is in kinetic form (which we vary throughout this work). The portion of mass, momentum and total energy each cell receives (in the rest frame of the star particle) is then

$$\Delta m_i = |\bar{\mathbf{w}}_i| m_{\text{ej}} \quad (10)$$

$$\Delta \mathbf{p}_i = \bar{\mathbf{w}}_i p_{\text{tot}} \quad (11)$$

$$\Delta E_i = |\bar{\mathbf{w}}_i| E_{\text{SN}}. \quad (12)$$

Transforming back to the simulation frame (i.e. the rest frame of the simulated volume), the momentum and energy fluxes become

$$\Delta \mathbf{p}'_i = \Delta \mathbf{p}_i + \Delta m_i \mathbf{v}_* \quad (13)$$

$$\Delta E'_i = \Delta E_i + \frac{1}{2\Delta m_i} \left(|\Delta \mathbf{p}'_i|^2 - |\Delta \mathbf{p}_i|^2 \right), \quad (14)$$

where \mathbf{v}_* is the velocity of the star particle in the simulation frame. Note that this implicitly deals with any momentum cancellation, i.e. the ‘lost’ kinetic energy becomes thermal energy.

The host cell receives the following mass and energy

$$\Delta m_{\text{host}} = f_{\text{host}} m_{\text{ej}} \quad (15)$$

$$\Delta E_{\text{host}} = f_{\text{host}} E_{\text{SN}} + \frac{1}{2} f_{\text{host}} m_{\text{ej}} |\mathbf{v}_* - \mathbf{v}_{\text{host}}|^2. \quad (16)$$

The final term in equation (16) assumes complete thermalisation of the kinetic energy carried by the star particle. Empirically, we find that the mean number of neighbouring

cells is ~ 20 . We therefore adopt $f_{\text{host}} = 5\%$ to evenly distribute feedback quantities. In practice, we find a very weak dependence on the value of f_{host} . In simulations described as containing no feedback, the host cell and neighbours receive mass and metals as described above but their energy and momentum are not altered. We adopt $m_{\text{ej}} = 10 M_{\odot}$, of which $2 M_{\odot}$ is in metals (i.e. a metallicity of 0.2), and $E_{\text{SN}} = 10^{51}$ ergs throughout this work.

2.4.1 Classical feedback schemes

For the purpose of this work, we refer to schemes that employ a simple dump of thermal and/or kinetic energy as classical feedback schemes. These use the methods outlined above with some value of f_{kin} . For pure thermal feedback, we use $f_{\text{kin}} = 0$. For pure kinetic feedback², we use $f_{\text{kin}} = 1$. We also trial a mixed feedback scheme that uses $f_{\text{kin}} = 0.28$, which distributes the energy into the ratio expected during the Sedov-Taylor phase (e.g. see Ostriker & McKee (1988); Cioffi et al. (1988) for analytical arguments, also see Kim & Ostriker (2015) for an example of this in a numerical simulation).

2.4.2 Delayed Cooling

Additionally to the classical feedback schemes we adopt a feedback prescription based on the delayed cooling method of Teyssier et al. (2013). This method aims to take into account (sub-grid) non-thermal processes that might store some of the feedback energy, such as, for example, unresolved turbulence, magnetic fields and cosmic rays. The timescales on which these processes dissipate energy is longer than the cooling time of the thermal component, so energy may be stored for longer and released gradually. We introduce a new variable u_{FB} which is used to record the energy density from feedback that gas particles currently possess and is advected with the gas flow, acting as a passive Lagrangian tracer (which is to say it is not directly involved in the hydrodynamics). When a gas cell is involved in a SN event, feedback energy is injected as described above with $f_{\text{kin}} = 0$ (i.e. entirely thermally apart from the momentum conserved from the star particle). The amount of energy received is also added to u_{FB} . This feedback energy store is allowed to dissipate as

$$\frac{du_{\text{FB}}}{dt} = -\frac{u_{\text{FB}}}{t_{\text{diss}}}, \quad (17)$$

where t_{diss} is some dissipation timescale as in Teyssier et al. (2013). Note that u_{FB} can also be increased if the gas cell is involved in another SN event. We compute an effective velocity dispersion corresponding to the feedback energy,

$$\sigma_{\text{FB}} = \sqrt{2u_{\text{FB}}}, \quad (18)$$

and the gas particle is not allowed to cool if this velocity dispersion is above some threshold. Following Teyssier et al. (2013) we use

$$\Lambda = 0 \text{ if } \sigma_{\text{FB}} > 10 \text{ km s}^{-1}. \quad (19)$$

² This should not be confused with other schemes sometimes referred to as ‘kinetic’ that boost the momentum input by some fixed mass loading factor (see Dubois & Teyssier 2008; Kimm et al. 2015; Rosdahl et al. 2017).

The motivation for switching off cooling when σ_{FB} is above this threshold is to mimic a non-thermal contribution to the pressure. Once the non-thermal contribution becomes comparable to the thermal contribution, cooling is allowed to continue as normal. We also trial a larger threshold value of 100 km s^{-1} in Appendix C.

We use a fixed value for the dissipation time of 10 Myr, as in Teysier et al. (2013). We also trial a variable dissipation time, based on the effective crossing time for the turbulence within a cell,

$$t_{\text{diss}} = \frac{\Delta x}{\sigma_{\text{FB}}}, \quad (20)$$

where Δx is the diameter of the cell.

2.4.3 Mechanical feedback

In this feedback scheme we aim to account for the PdV work done during the Sedov-Taylor phase of the SNe remnant expansion, where the momentum can be boosted by around an order of magnitude. The correct momentum to couple to the ISM therefore depends on the stage of the expansion (alternatively parametrized in terms of swept up mass), limited by the final momentum at the point when the remnant exists the Sedov-Taylor phase. Several such schemes exist in the literature (see e.g. Hopkins et al. 2014, 2017; Hopkins et al. 2018; Kimm & Cen 2014; Kimm et al. 2015; Martizzi et al. 2015). In our mechanical feedback scheme, momentum calculated in equation (13) is enhanced as follows

$$\Delta \mathbf{p}'_i = \Delta \mathbf{p}'_i \text{MIN} \left[\sqrt{1 + \frac{m_i}{\Delta m_i} \frac{p_{\text{fin}}}{p_{\text{tot}}}} \right], \quad (21)$$

where p_{fin} is the momentum as the remnant transitions to the snowplough phase (Blondin et al. 1998; Thornton et al. 1998; Geen et al. 2015; Kim & Ostriker 2015; Martizzi et al. 2015); following Kimm et al. (2015) we adopt

$$p_{\text{fin}} = 3 \times 10^5 \text{ km s}^{-1} M_{\odot} E_{51}^{16/17} n_{\text{H}}^{-2/17} Z'^{-0.14}, \quad (22)$$

where $E_{51} = (E_{\text{SN}}/10^{51} \text{ ergs}) = N_{\text{SN}}$, n_{H} is the hydrogen number density and $Z' = \text{MAX}(Z/Z_{\odot}, 0.01)$ is the metallicity in solar units. Note that we calculate $\Delta \mathbf{p}'_i$ for each cell involved in the SN event *independently*.

3 SIMULATIONS

3.1 Initial conditions and simulation details

We simulate isolated galaxies comprising of a stellar and gas disk, a stellar bulge, a hot gaseous atmosphere and a static background potential representing the dark matter component. The dark matter follows an NFW profile (Navarro et al. 1997) with concentration parameter $c = 10$ and spin parameter $\lambda = 0.04$ for all galaxies simulated. The baryonic component is generated using MAKENEWDISK (Springel et al. 2005). The disk density profile is exponential in radius. The stellar disk has a Gaussian vertical density profile with a scale height 0.1 times the scale radius. The stellar bulge has a scale length 0.1 times the scale radius of the disk. The collisionless particles comprising the stellar disk and bulge in the initial conditions do not contribute to stellar feedback. The vertical structure of the gas disk is determined so as to obtain initial hydrostatic equilibrium.

We simulate three galaxies in this work with properties

Table 1. Initial conditions of the three disk galaxies modelled in this work, referred to as ‘Small’, ‘Fiducial’ and ‘Large’. We list the total mass of the galaxy, M_{tot} , (excluding the CGM, which is negligible), the halo virial radius, R_{vir} , the mass in the disk component, M_{disk} , the fraction of the disk component in gas, f_{gas} , the scale radius of the disk, r_{s} , the scale height of the stellar disk, h_{s} , the mass of the stellar bulge, M_{bulge} , the initial metallicity of the gas in the disk, Z_{disk} , (the CGM initially contains no metals), the initial temperature of the disk, T_{disk} .

| | Small | Fiducial | Large |
|--------------------|-----------------------------|-----------------------------|-----------------------------|
| M_{tot} | $10^9 M_{\odot}$ | $10^{10} M_{\odot}$ | $10^{11} M_{\odot}$ |
| R_{vir} | 16.3 kpc | 35.0 kpc | 75.5 kpc |
| M_{disk} | $3.5 \times 10^7 M_{\odot}$ | $3.5 \times 10^8 M_{\odot}$ | $3.5 \times 10^9 M_{\odot}$ |
| f_{gas} | 0.5 | 0.5 | 0.5 |
| r_{s} | 0.33 kpc | 0.70 kpc | 1.52 kpc |
| h_{s} | 33 pc | 70 pc | 152 pc |
| M_{bulge} | $3.5 \times 10^6 M_{\odot}$ | $3.5 \times 10^7 M_{\odot}$ | $3.5 \times 10^8 M_{\odot}$ |
| Z_{disk} | $0.1 Z_{\odot}$ | $0.1 Z_{\odot}$ | $0.1 Z_{\odot}$ |
| T_{disk} | $2.1 \times 10^3 \text{ K}$ | 10^4 K | $4.6 \times 10^4 \text{ K}$ |

described in Table 1. The majority of simulations in this work are of a galaxy with a total mass of $10^{10} M_{\odot}$. We refer to this setup as the fiducial galaxy. This setup is comparable to the G8 model in Rosdahl et al. (2015). We also simulate two additional systems, ‘Small’ and ‘Large’, which are an order of magnitude lower and higher in mass, respectively. For our fiducial model, we initialise the disk with a temperature of 10^4 K . We scale the initial disk temperature with the virial temperature of the halo for the ‘Small’ and ‘Large’ models. This is to avoid an initially vertically diffuse disk for the ‘Small’ model, while also maintaining consistency between the models³. The gas in the disk is initialised with a metallicity of $Z = 0.1 Z_{\odot}$. To roughly represent the CGM we include a hot gas atmosphere of uniform density $n_{\text{H}} = 10^{-6} \text{ cm}^{-3}$, uniform temperature 10^6 K and zero metallicity.

Gas cells and star particles (both those present in the initial conditions and newly created stars) share the same mass, $2000 M_{\odot}$, $200 M_{\odot}$ and $20 M_{\odot}$ for the low, intermediate and high resolution runs, respectively. At the highest resolution, the mass of cells/star particles approaches that of the total ejecta mass per SN ($10 M_{\odot}$). We have confirmed that the refinement/derefinement scheme in place in AREPO is sufficiently effective such that star particles always have enough mass to provide the full ejecta mass budget in all but a negligible fraction of SN events ($\lesssim 1\%$). Table 2 contains details of every simulation presented in the main body of this work (i.e. not including simulations presented in the appendices), including the galaxy model used, the resolution and number of cells/particles, gravitational softenings, additional star formation and feedback parameters and the mass of new stars formed after 250 Myr.

3.2 Disk morphologies and gas phases

Fig. 1 shows face-on and edge-on projections of the gas and newly formed stars in the highest resolution simulations after 250 Myr. Without feedback, the gas disk cools efficiently

³ While the disks will rapidly cool once the simulation start and the vertical structure will settle into an equilibrium configuration, we find that if the initial disk structure is too vertically diffuse in the ‘Small’ model, the resulting collapse is too severe and does not allow the disk to settle satisfactorily.

Table 2. Details of all simulations presented in this work. From left to right we list: galaxy model used (see Table 1), feedback method used (and any additional information), target mass of gas cells (and star particles), number of gas cells (excluding CGM) and star particles in the initial conditions, cell diameter at the star formation density threshold of 10 cm^{-3} (note that due to our Lagrangian method, cells can become much smaller, with $\Delta x \propto \rho^{-1/3}$), minimum gravitational softening for gas cells (and fixed softening for star particles), feedback and star formation parameters, and total newly formed stellar mass present at 250 Myr (not including stellar mass returned to the ISM through feedback).

| Galaxy | Feedback | $m_{\text{cell}} [M_{\odot}]$ | N_{part} | $\Delta x_{\text{SF}} [\text{pc}]$ | $\epsilon_{\text{min}} [\text{pc}]$ | Parameters | $M_* [10^7 M_{\odot}]$ |
|----------|--|-------------------------------|---------------------|------------------------------------|-------------------------------------|--|------------------------|
| Fiducial | None | 2000 | 1.925×10^5 | 22.7 | 8.1 | - | 7.64 |
| Fiducial | Thermal | 2000 | 1.925×10^5 | 22.7 | 8.1 | $f_{\text{kin}} = 0.0$ | 6.82 |
| Fiducial | Mixed | 2000 | 1.925×10^5 | 22.7 | 8.1 | $f_{\text{kin}} = 0.28$ | 6.63 |
| Fiducial | Kinetic | 2000 | 1.925×10^5 | 22.7 | 8.1 | $f_{\text{kin}} = 1.0$ | 5.82 |
| Fiducial | Delayed cooling | 2000 | 1.925×10^5 | 22.7 | 8.1 | $f_{\text{kin}} = 0.0, \sigma_{\text{thresh}} = 10 \text{ km s}^{-1}$ $t_{\text{diss}} = 10 \text{ Myr}$ | 0.18 |
| Fiducial | Delayed cooling (variable t_{diss}) | 2000 | 1.925×10^5 | 22.7 | 8.1 | $f_{\text{kin}} = 0.0, \sigma_{\text{thresh}} = 10 \text{ km s}^{-1}$ $t_{\text{diss}} = \Delta x / \sigma_{\text{FB}}$ | 0.40 |
| Fiducial | Mechanical | 2000 | 1.925×10^5 | 22.7 | 8.1 | $f_{\text{kin}} = 1.0$ | 1.43 |
| Fiducial | None | 200 | 1.925×10^6 | 10.6 | 3.8 | - | 9.56 |
| Fiducial | Thermal | 200 | 1.925×10^6 | 10.6 | 3.8 | $f_{\text{kin}} = 0.0$ | 8.64 |
| Fiducial | Mixed | 200 | 1.925×10^6 | 10.6 | 3.8 | $f_{\text{kin}} = 0.28$ | 8.39 |
| Fiducial | Kinetic | 200 | 1.925×10^6 | 10.6 | 3.8 | $f_{\text{kin}} = 1.0$ | 7.93 |
| Fiducial | Delayed cooling | 200 | 1.925×10^6 | 10.6 | 3.8 | $f_{\text{kin}} = 0.0, \sigma_{\text{thresh}} = 10 \text{ km s}^{-1}$ $t_{\text{diss}} = 10 \text{ Myr}$ | 0.21 |
| Fiducial | Delayed cooling (variable t_{diss}) | 200 | 1.925×10^6 | 10.6 | 3.8 | $f_{\text{kin}} = 0.0, \sigma_{\text{thresh}} = 10 \text{ km s}^{-1}$ $t_{\text{diss}} = \Delta x / \sigma_{\text{FB}}$ | 0.59 |
| Fiducial | Mechanical | 200 | 1.925×10^6 | 10.6 | 3.8 | $f_{\text{kin}} = 1.0$ | 1.02 |
| Small | None | 200 | 1.925×10^5 | 10.6 | 3.8 | - | 0.082 |
| Small | Mechanical | 200 | 1.925×10^5 | 10.6 | 3.8 | $f_{\text{kin}} = 1.0$ | 0.014 |
| Large | None | 200 | 1.925×10^7 | 10.6 | 3.8 | - | 124.1 |
| Large | Mechanical | 200 | 1.925×10^7 | 10.6 | 3.8 | $f_{\text{kin}} = 1.0$ | 42.6 |
| Fiducial | None (High SF efficiency) | 200 | 1.925×10^6 | 10.6 | 3.8 | $\epsilon_{\text{SF}} = 15\%$ | 11.9 |
| Fiducial | Mechanical (High SF efficiency) | 200 | 1.925×10^6 | 10.6 | 3.8 | $\epsilon_{\text{SF}} = 15\%, f_{\text{kin}} = 1.0$ | 1.33 |
| Fiducial | None (High SF density threshold) | 200 | 1.925×10^6 | 10.6 | 3.8 | $n_{\text{SF}} = 100 \text{ cm}^{-3}$ | 10.1 |
| Fiducial | Mechanical (High SF density threshold) | 200 | 1.925×10^6 | 10.6 | 3.8 | $n_{\text{SF}} = 100 \text{ cm}^{-3}, f_{\text{kin}} = 1.0$ | 1.43 |
| Fiducial | None | 20 | 1.925×10^7 | 4.9 | 1.8 | - | 9.23 |
| Fiducial | Thermal | 20 | 1.925×10^7 | 4.9 | 1.8 | $f_{\text{kin}} = 0.0$ | 1.09 |
| Fiducial | Mixed | 20 | 1.925×10^7 | 4.9 | 1.8 | $f_{\text{kin}} = 0.28$ | 0.94 |
| Fiducial | Kinetic | 20 | 1.925×10^7 | 4.9 | 1.8 | $f_{\text{kin}} = 1.0$ | 0.92 |
| Fiducial | Delayed cooling | 20 | 1.925×10^7 | 4.9 | 1.8 | $f_{\text{kin}} = 0.0, \sigma_{\text{thresh}} = 10 \text{ km s}^{-1}$ $t_{\text{diss}} = 10 \text{ Myr}$ | 0.27 |
| Fiducial | Delayed cooling (variable t_{diss}) | 20 | 1.925×10^7 | 4.9 | 1.8 | $f_{\text{kin}} = 0.0, \sigma_{\text{thresh}} = 10 \text{ km s}^{-1}$ $t_{\text{diss}} = \Delta x / \sigma_{\text{FB}}$ | 0.79 |
| Fiducial | Mechanical | 20 | 1.925×10^7 | 4.9 | 1.8 | $f_{\text{kin}} = 1.0$ | 0.72 |

and adopts a highly clumpy morphology on large scales. The gas in these clumps is extremely efficient at forming stars. Hence, the distribution of newly formed stars also follows this clumped morphology. There is no single dominant bulge component, instead there are multiple large clumps near the centre of the disk. Seen edge-on, the gas disk is very thin as, having cooled, it lacks vertical pressure support. The morphology for the simulations without feedback is similar to those carried out at lower resolutions (see Appendix D).

The thermal, mixed (not shown) and kinetic feedback schemes are able to prevent the formation of gas clumps, instead forming complex structures of dense gas and spiral arms. This structure is also reflected in the disk of newly

formed stars. The multiple clumps of stars seen in the no feedback case are not present, though there is a definite overdensity of new stars in the centre of the disk. The global surface density of newly formed stars is greatly reduced (see Section 3.3). Seen edge-on, a complex vertical gas structure is evident with outflows present. At lower resolutions, this morphology is not evident (see Appendix D, Figs. D1 and D2 for equivalent projections). Instead, the thermal, mixed and kinetic feedback schemes are unable to prevent the formation of dense clumps of gas. The subsequent evolution of the disk is then broadly similar to that of the runs without feedback. This clearly indicates that a mass resolution

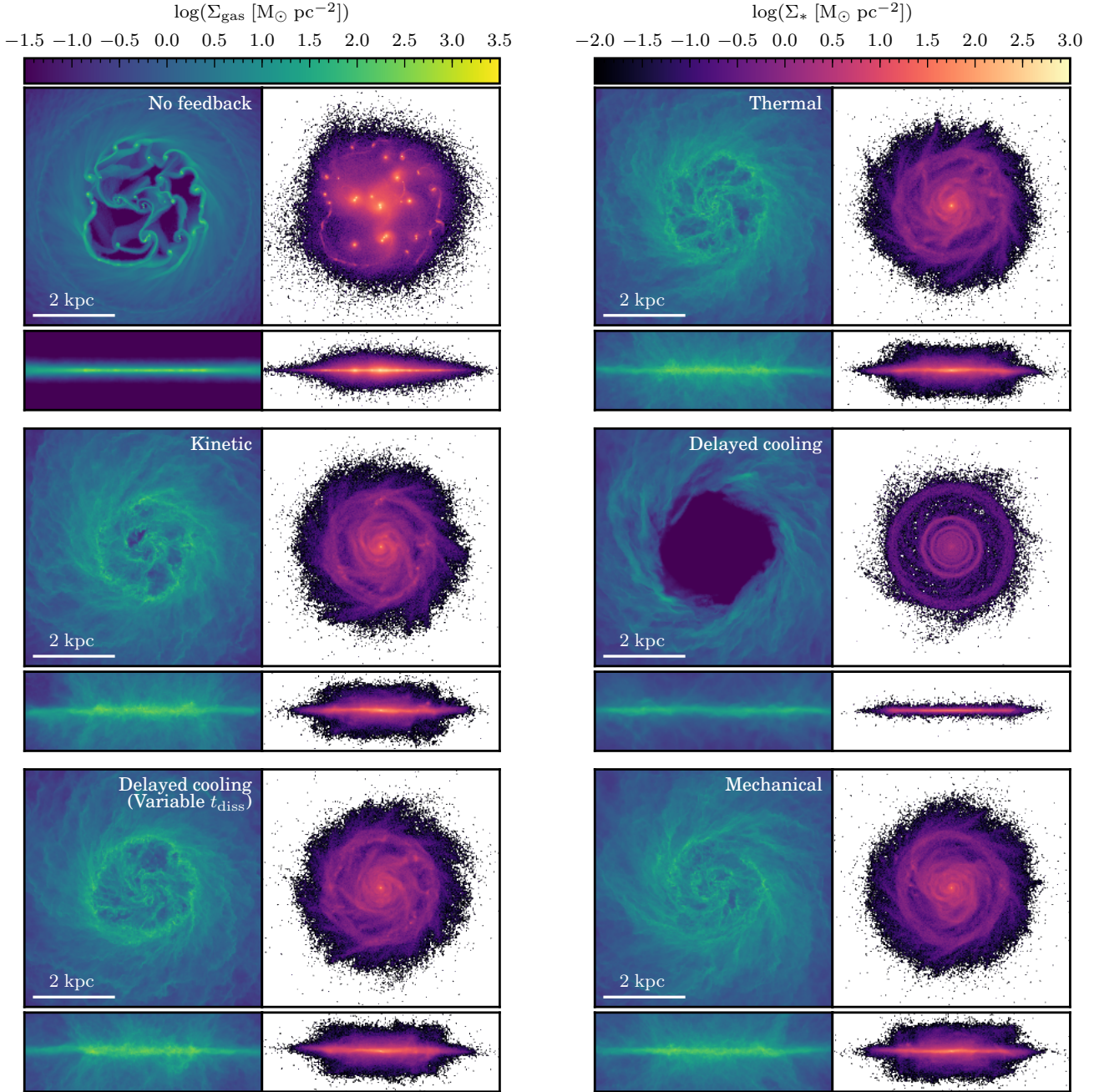


Figure 1. Projections of gas and newly formed stars at 250 Myr for different feedback runs at $20 M_{\odot}$ resolution, viewed both face-on and edge-on. The mixed feedback simulation is not shown as the results are similar to the thermal and kinetic feedback simulations. The simulation without feedback results in dense clumps of gas which produce stars at a high rate. The simulations with classical, delayed cooling with variable t_{diss} and mechanical feedback schemes are able to suppress the formation of dense clumps and reduce the mass of stars formed. They all show very similar disk morphologies with gas and stars exhibiting spiral patterns. The delayed cooling scheme is far too effective and blows up a large fraction of the gaseous disk leading to ring-like structures of newly formed stars. Equivalent plots for the lower resolution simulations can be found in Appendix D, Figs. D1 and D2.

of at least $\sim 20 M_{\odot}$ is needed for these feedback schemes to become effective.

The simulation with delayed cooling using a fixed dissipation time results in a completely disrupted disk. When the first SNe occur, they are able to eject most of the gas from the centre, leaving behind a central, low density region

at 250 Myr, as evident in Fig. 1. The projection of newly formed stars shows an unusual ring-like structure. This is caused by the violent ejection of gas from the centre, forming stars in areas of compression as the resulting shock is transmitted through the disk plane, essentially leading to a ‘positive’ feedback. This behaviour is also apparent in the

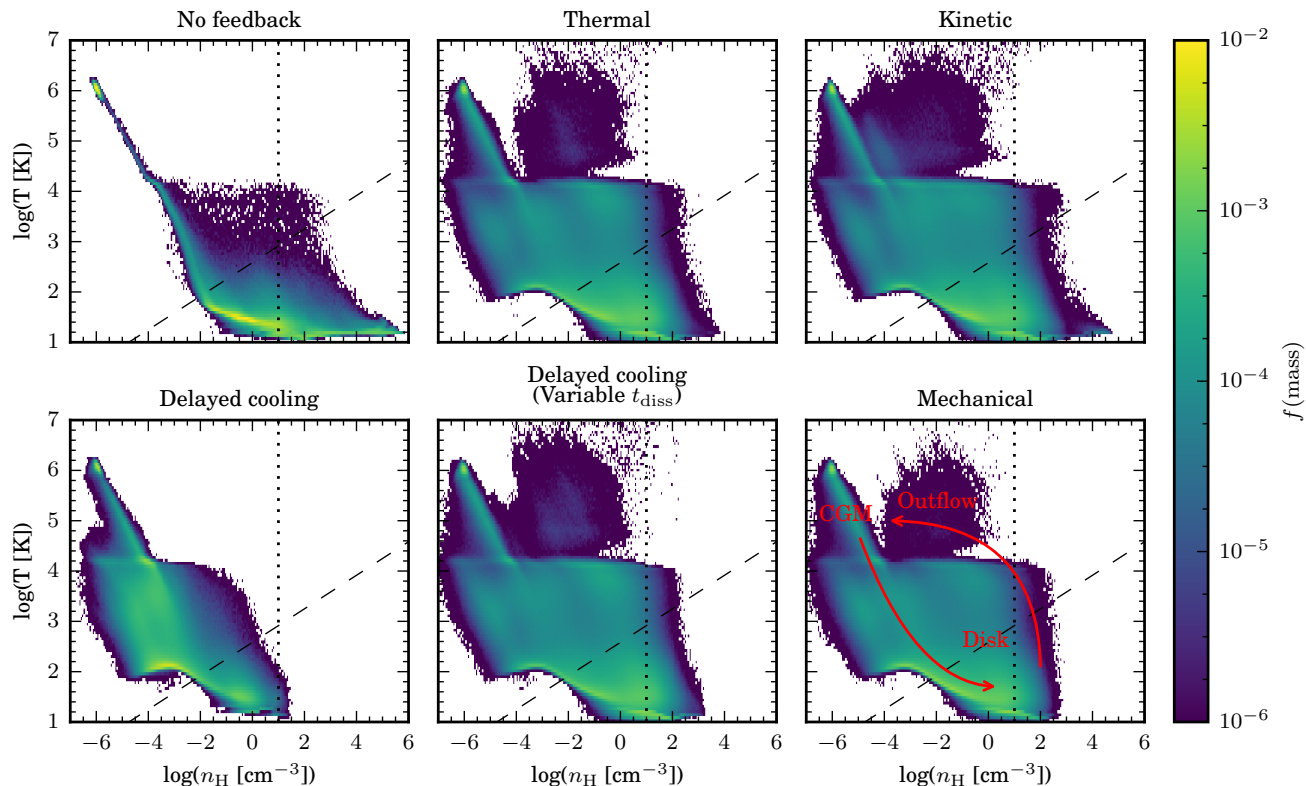


Figure 2. Phase diagram for gas within the virial radius at 250 Myr for different feedback simulations at $20M_{\odot}$ resolution. Colour coding is according to the fraction of mass in a given pixel. The vertical dotted line shows the star formation density threshold, n_{SF} . The region of the phase diagram below the diagonal dashed line is where the pressure is dominated by the non-thermal Jeans pressure floor, rather than conventional thermal pressure. The mixed feedback simulation is not shown as the results are similar to the thermal and kinetic feedback simulations. While the majority of gas resides at low temperature and high densities, i.e. within the disk, all feedback models are able to remove a fraction of gas from the ISM and to heat it to high temperatures above 10^4 K launching galaxy-scale outflow. The delayed cooling launches a large outflow at early times, the majority of which is outside the virial radius at 250 Myr. The plot for the mechanical feedback simulation is labelled, showing the location of disk (gas denser than 10^{-4} cm^{-3} is within 3 scale radii and heights), outflowing material (the region marked on the plot is all outflowing at more than 50 km s^{-1} , but still within the disk region) and the CGM on the phase diagram. Also marked is the circulation of gas around the diagram due to the galactic fountain effect.

lower resolution simulations but can largely be regarded as a numerical artifact. The strength of the feedback, and resulting gas and stellar morphologies, indicate that the choice of parameters for this scheme is not appropriate and further tuning is necessary. Further discussion of the issues with the delayed cooling in our simulation can be found later and simulations carried out with different parameters can be found in Appendix C.

The delayed cooling run with variable dissipation time ($t_{\text{diss}} = \Delta x / \sigma_{\text{FB}}$) is not as strong. The disk morphology is similar to the thermal, mixed and kinetic feedback schemes at this resolution, with suppression of large scale clumping without destruction of the disk. However, perhaps counter-intuitively, this feedback scheme becomes stronger at lower resolutions (as evidenced by Figs. D1 and D2), disrupting the disk in the $2000 M_{\odot}$ simulation. This is because the dependence on the cell diameter results in very short dissipation times at high resolution. At our highest resolution of $20 M_{\odot}$, the cooling is essentially not delayed at all, resulting in a straight thermal dump and hence similarity to the classic thermal feedback scheme. Qualitatively, this is the desired behaviour, with the delayed cooling being re-

duced at resolutions high enough to resolve the Sedov-Taylor phase, but increased at lower resolution. However, the lack of convergence with resolution (and disk destruction at low resolution) indicates some form of tunable parameter might need to be introduced to refine this scheme.

Finally, the mechanical feedback scheme results in morphologies similar to the classical feedback schemes. Uniquely among the schemes tested, the mechanical feedback is able to produce these morphologies across two orders of magnitude in resolution. While the classical feedback schemes overcool at lower resolutions, the mechanical feedback scheme is still able to suppress large scale clumping and the formation of high density gas, without destroying the disk. Unlike the variable dissipation time delayed cooling scheme, the implicit modulation of small scale feedback strength as a function of resolution in the mechanical scheme is able to produce convergent disk morphologies at our three resolutions.

Fig. 2 shows phase diagrams for the gas in the highest resolution simulations at 250 Myr (similar plots for the lower resolution runs may be found in Appendix D). In the no feedback simulation, the majority of the gas in the disk has cooled well below 10^2 K and there is a substantial quan-

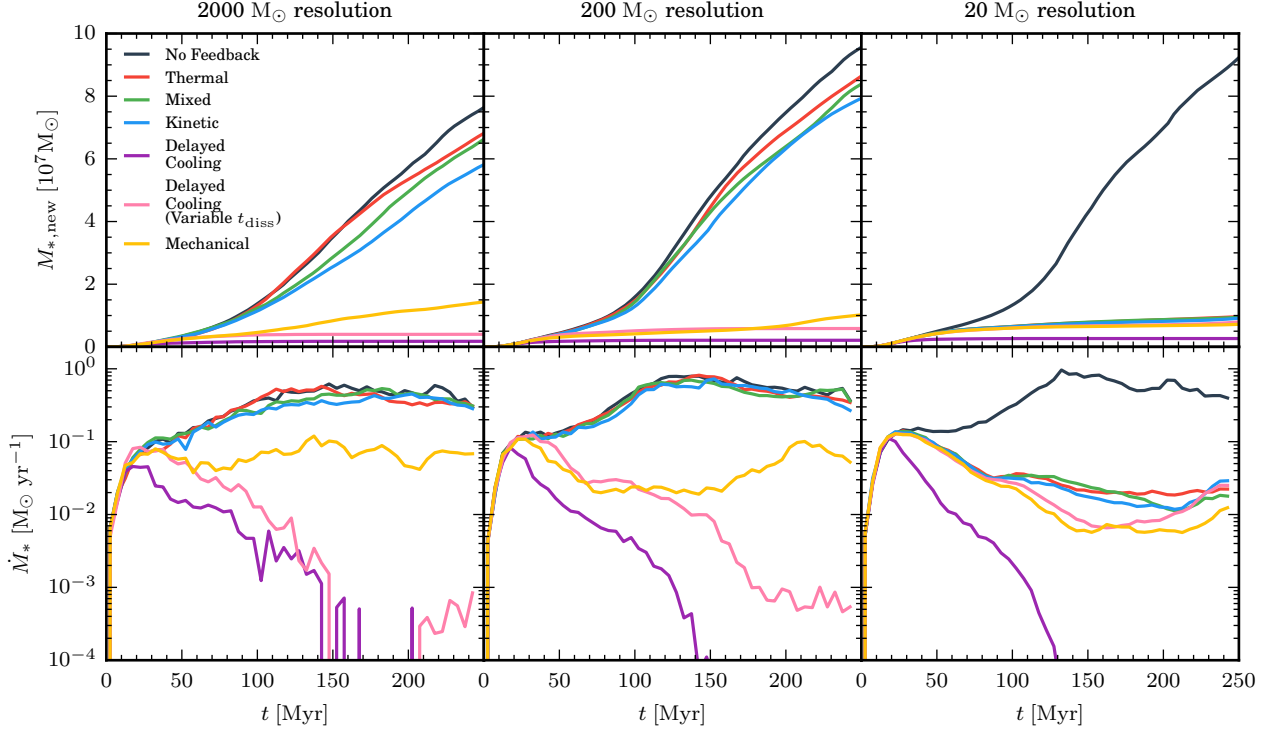


Figure 3. Newly formed stellar mass (top) and SFRs (bottom) for our three resolutions. At the low and intermediate resolutions, the classical feedback schemes experience the overcooling problem and barely suppress star formation relative to the no feedback simulations. However, at the highest resolution they are able to suppress star formation. The delayed cooling schemes are in general too powerful, completely quenching star formation (with the exception of the highest resolution variable t_{diss} run which is barely delaying cooling in this regime). The mechanical feedback scheme suppresses star formation by a similar amount across all three resolutions, demonstrating reasonable convergence, while also being comparable to the classical schemes at the highest resolution, suggesting it is converging onto the ‘correct’ physical result.

tity of gas at high density, as far as $\sim 10^6 \text{ cm}^{-3}$. Once the gas enters this cold, dense phase, the resulting evolution is regulated by the non-thermal pressure floor and is highly dependent on the choice of parameters (for more details see Appendix A), though our results are qualitatively similar to comparable simulations in the literature (e.g. Rosdahl et al. 2015, 2017; Hu et al. 2016, 2017). At lower resolution, the results are similar, though gas does not reach quite such high densities, an expected consequence of lower resolution. At the highest resolution, the classical feedback schemes are able to maintain a warm phase in the disk. While cold, dense gas is still present it does not reach the high densities seen in the no feedback simulation. An additional component of gas is apparent on the phase diagrams, between $T \sim 10^4 - 10^7 \text{ K}$ and $n \sim 10^{-5} - 10 \text{ cm}^{-3}$. This is gas that has received feedback energy and is expanding up out of the plane of the disk. When viewed as a function of time, a cyclical pattern anticlockwise around the phase diagram may be observed with gas cooling and contracting to star forming densities (moving down and right), being heated by feedback (moving up), expanding (moving left). Gas which rains back on the disk (the so-called galactic fountain, see Section 3.3) cools and drops back down the phase diagram and may enter the cycle again.

The phase diagram for the delayed cooling with fixed dissipation time feedback at 250 Myr shows a complete ab-

sence of dense gas. In addition, because the feedback has efficiently quenched star formation (see Section 3.3), there are no further SNe after the initial budget has been exhausted. This results in the lack of gas above 10^4 K (with the exception of that in the CGM). When the delayed cooling scheme is used with a variable dissipation time, at the highest resolution the phase diagrams are similar to those for the classical schemes. However, at lower resolution as the feedback becomes stronger, they become similar to the delayed cooling with fixed dissipation time. In the highest resolution simulation, the mechanical feedback scheme produces phase diagrams similar to the classical schemes, although the highest density gas has been curtailed. The phase diagrams look similar across all resolutions.

3.3 Star formation rates and outflows

Fig. 3 shows the mass of stars formed and the star formation rates as a function of time for all feedback schemes at all three resolutions. The no feedback simulations are similar across all three resolutions. As gas cools and reaches star forming densities, star formation begins. After a sudden jump in star formation at the beginning of the simulation, the SFR rises gradually to a roughly constant rate $\sim 0.2 - 1 \text{ M}_\odot \text{ yr}^{-1}$. The higher resolutions result in denser clump formations leading to slightly higher SFR on average, but the total stellar mass formed is similar between the three resolutions ($7.64 \times 10^7 \text{ M}_\odot$, $9.56 \times 10^7 \text{ M}_\odot$ and

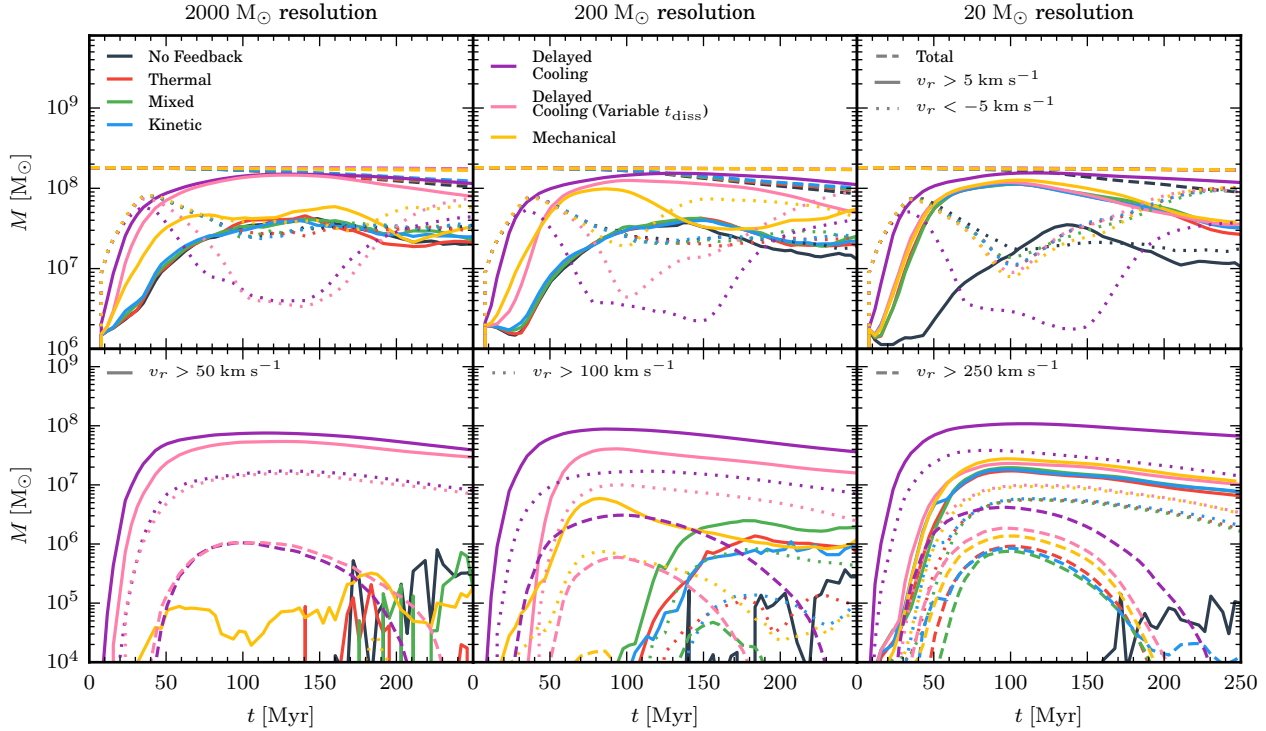


Figure 4. Mass of gas moving at various radial velocities within the virial radius as a function of time for our different feedback schemes at all three resolutions. *Top:* Total gas mass within the virial radius (dashed curves), mass of gas radially outflowing and inflowing over 5 km s^{-1} (solid and dotted curves, respectively). *Bottom:* mass of gas radially outflowing at more than 50, 100 and 250 km s^{-1} (solid, dotted and dashed curves, respectively). Mass of the outflowing gas is very sensitive to the resolution of simulations and only in the highest resolution runs do feedback schemes launch significant outflows.

$9.23 \times 10^7 M_{\odot}$ for the $2000 M_{\odot}$, $200 M_{\odot}$, and $20 M_{\odot}$ resolutions, respectively). It should be noted that in the absence of effective feedback, the SFR and its time dependence become regulated by the choice of non-thermal pressure floor since that impacts the scale of fragmentation and the densities reached. However, our scaling of the pressure floor with resolution (as described in Section 2.2) results by construction in reasonably convergent behaviour with resolution, though it is not convergent with choice of pressure floor parameter (see Appendix A).

In the lower resolution simulations, the classical feedback schemes are unable to suppress star formation by more than $\sim 20\%$ in the best case as they catastrophically overcool and follow the same behaviour as the no feedback simulations. A slight trend of increased effectiveness with increased f_{kin} is apparent but the total impact on SFRs is weak. However, at our highest resolution of $20 M_{\odot}$, the classical feedback schemes become effective, reducing SFR and total stellar mass by around an order of magnitude with respect to the no feedback simulations.

The delayed cooling scheme with a fixed dissipation time efficiently quenches star formation with a single period of SNe activity, expelling all star forming gas from the centre of the system. The results are well converged with resolution, forming almost exactly the same stellar mass. The total stellar mass formed is only a few percent of the no feedback case. As described in the previous section, the delayed cooling with variable dissipation time results in stronger feed-

back at lower resolution. This can be seen in Fig. 3 where the SFR is similar to the fixed dissipation time simulation at $2000 M_{\odot}$, higher at $200 M_{\odot}$ and close to the classical schemes at $20 M_{\odot}$.

At the lowest resolution, the mechanical feedback scheme results in a steady star formation rate below $10^{-1} M_{\odot} \text{ yr}^{-1}$, suppressing total stars formed by approximately a factor of 5. With increasingly higher resolution, the SFRs are suppressed slightly more, but encouragingly the total stellar mass formed is within a factor of 2 from the lowest to the highest resolution simulations. The SFR exhibits a slight dip in the $200 M_{\odot}$ resolution simulations, increasing slightly towards 200 Myr. This is due to a ‘galactic fountain’ effect, with gas launched from the disk returning and forming new stars, which we discuss in greater detail below. At the highest resolution, the mechanical feedback scheme is reasonably similar to the classical schemes because the Sedov-Taylor phase is resolved in the majority of SNe events, so the momentum boost factor is close to unity. The mechanical scheme is slightly stronger than the classical schemes due to the few SNe at this resolution that are not sufficiently resolved by the classical schemes because they occur at high densities (for further details see Section 3.5).

While the general features of SFRs are converged for feedback schemes that do not overcool across different resolutions, such as the ‘Mechanical’ run, interestingly the same is not true for outflows (with the exception of delayed cooling runs, which drive strong outflows at all resolutions). Fig. 4

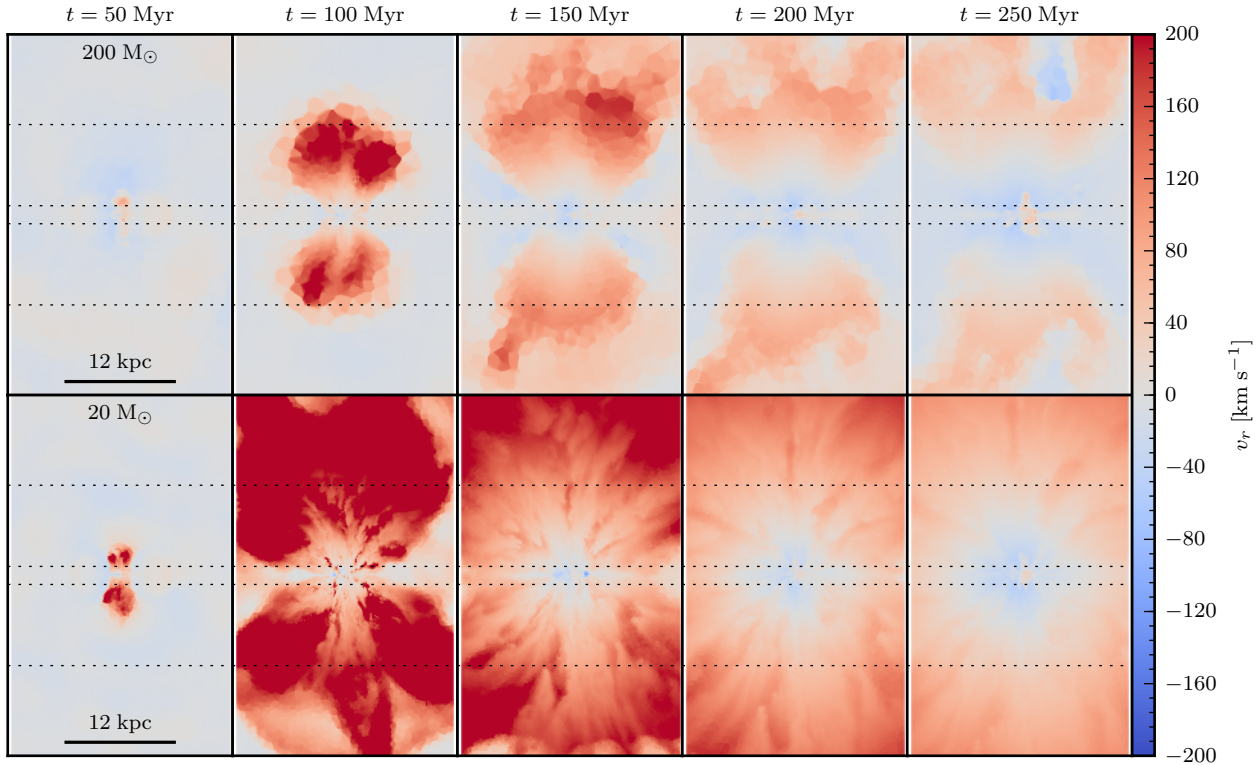


Figure 5. Slices through the centre of the mechanical feedback simulation at $200 M_{\odot}$ (top) and $20 M_{\odot}$ (bottom) resolutions showing radial velocity at various times (outflowing gas is in red, while the inflowing gas is in blue). The horizontal dotted lines show the planes at 1 and 10 kpc away from the midplane of the disk, used to examine the outflows in Fig. 6. Not only is the outflow stronger in the higher resolution run but the spatial structure of inflowing and outflowing gas changes as well with resolution, where the galactic fountain effect is more pronounced in the lower resolution simulation.

shows the total gas mass within the virial radius moving at various radial velocities for our various feedback schemes at three resolutions. In the no feedback run, the behaviour is simple and is essentially the same across all resolutions. Initially, there is a rise in gas inflow as the disk collapses vertically. Gas tagged as outflowing (moving more than 5 km s^{-1} radially outwards) is apparent despite the lack of feedback, but this is caused by motions in the disk rather than a true outflow. After $\sim 100 \text{ Myr}$, the inflow and outflow rates are approximately equal. The gas settles in the disk plane with small net motions due to the movements of the clumps and the gas reservoir is rapidly converted to stars. Note that in a cosmological context, there would be a constant net inflow from well outside the disk due to cosmic accretion. In our setup, the initially inflowing gas is simply the disk settling into an equilibrium configuration as it cools, our background uniform CGM has long cooling times, largely stays in place and does not accrete onto the disk.

The same behaviour is apparent for the classical feedback schemes at the lower two resolutions. Due to overcooling, the feedback is unable to suppress the inflowing gas, i.e. neither to stabilise the disk with a larger scale height nor to drive any appreciable outflows. At the lowest resolution, there is no gas outflowing faster than 100 km s^{-1} . There is a small fraction ($\sim 0.1 \%$ of the total gas mass) moving faster than 50 km s^{-1} at late times, but these are merely motions of the clumpy disk and are present in the no

feedback run. At the $200 M_{\odot}$ resolution, the feedback is able to generate some outflows faster than 50 km s^{-1} ($\sim 1 \%$ of the total gas mass) and a small amount moving faster than 100 km s^{-1} once the density in the disk has dropped slightly due to conversion of gas to stars, reducing the overcooling effect. However, this little mass moving at relatively low velocities is not able to make it far from the disk plane and the net inflow and outflow rates are still comparable. Despite significantly suppressing star formation in the lowest resolution simulation, mechanical feedback struggles to launch outflows. It generates marginally larger outflow rates than the classical feedback schemes, but the inflow and outflow rates match after 50 Myr. In the $200 M_{\odot}$ resolution simulation, the feedback is able to drive a much stronger outflow at early times, suppressing inflow and launching a significant mass of material faster than 50 km s^{-1} (and a smaller amount faster than 100 km s^{-1}). However, this material is not moving fast enough to escape the galaxy, so it returns back to the disk in a galactic fountain, with the inflow rates overtaking the outflow rates at around $\sim 125 \text{ Myr}$.

At the highest resolution, the classical and mechanical feedback schemes are relatively similar and are able to launch strong outflows. From around 50 Myr onwards, over $10^7 M_{\odot}$ of gas is moving faster than 50 km s^{-1} , the majority of which is moving faster than 100 km s^{-1} and a non-negligible fraction is moving faster than 250 km s^{-1} . The net outflow rates are approximately an order of magnitude

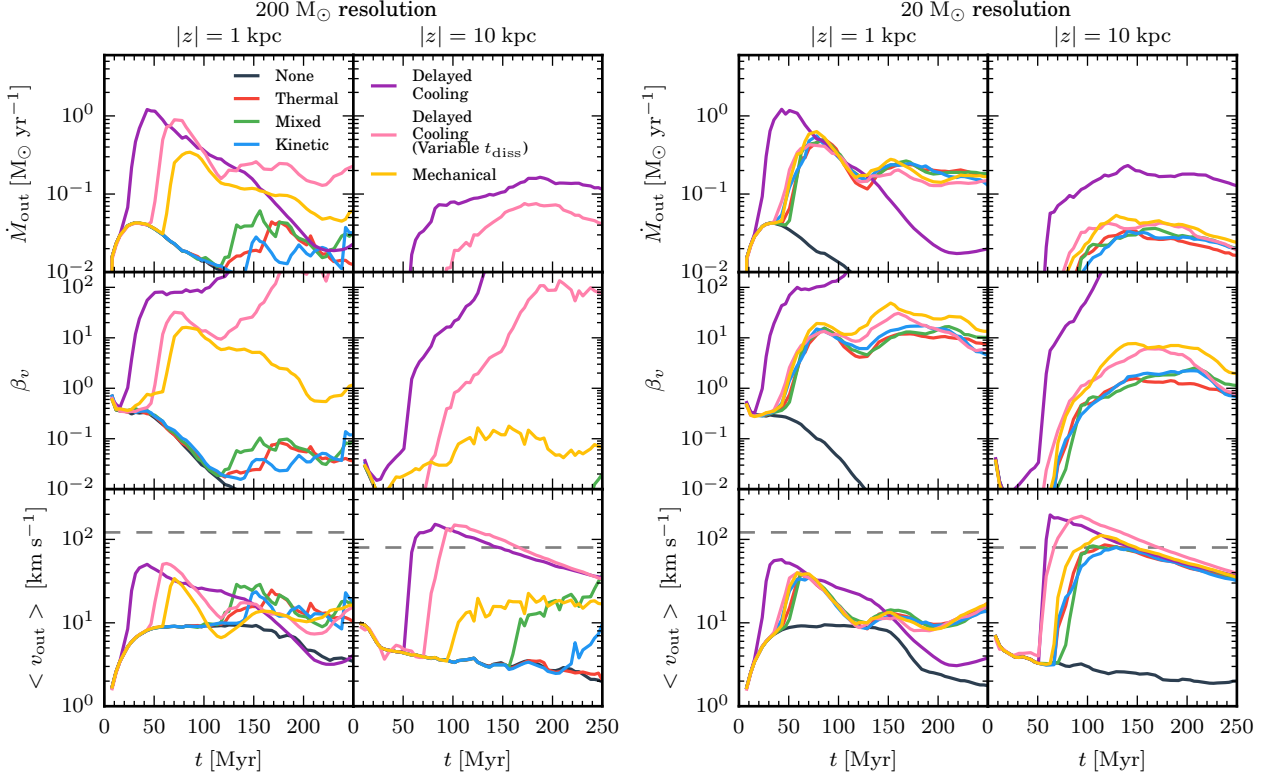


Figure 6. Mass outflow rates (top), mass loading factors (middle) and mass-weighted average outflow velocities (bottom) for our different feedback models across planes at 1 and 10 kpc from the disk midplane for our two highest resolution simulations (left and right panels). The dashed grey lines indicate the escape velocity at the relative disk height. The 2000 M_⊙ simulations are not shown as outflows for all except delayed cooling are negligible (see Figs. 4 and D3). Outflow velocities comparable to the escape velocity and mass loading factors of a few are only reached at the highest resolution simulations for all feedback runs (except for delayed cooling runs which are over-efficient).

larger than the inflow rates at 100 Myr. However, after this point, inflow rates rise and outflow rates drop slightly as the lower velocity gas begins to stall and flow inwards. At around 180 Myr, the inflow rates exceed the outflow rates. This galactic fountain effect can be seen in Fig. 5, which shows gas in a vertical slice through the system colour coded by radial velocity at several times for the mechanical feedback scheme at the higher two resolutions. In the top panel, in the 200 M_⊙ simulation, an outflow is launched at 50 Myr. As time progresses, the outflowing gas moves up away from the centre of the system, but gas begins to flow inwards, segregated by velocity. By 200 Myr, the centre is dominated by returning gas while only the fastest moving gas has continued to outflow. At 250 Myr, a new outflow has just been launched, resulting in a complex, interleaved pattern of gas outflowing, inflowing and outflowing with increasing height from the disk. At the higher resolution, the initial outflow is much faster. At 100 Myr and 150 Myr, the covering fraction of outflowing gas is much larger than in the lower resolution run with all but the very central regions dominated by outflows. A complex structure of outflowing gas is apparent, with a ‘finger’ like pattern of various outflow velocities. Again, at the final snapshot at 250 Myr, the central regions contain largely inflowing gas, but far more gas continues to outflow as compared to the lower resolution.

As previously discussed, the delayed cooling schemes

launch very strong outflows. As can be seen in Fig. 4, once again the delayed cooling with fixed dissipation time is extremely well converged across the three resolutions, drastically suppressing inflows and launching large quantities of gas at high velocities from essentially a single period of SNe activity (although, inflow rates begin to pick up at late times once SNe have been shut off due to star formation quenching). However, as previously mentioned, this feedback seems unphysically strong. The delayed cooling with variable dissipation time follows similar behaviour to the fixed dissipation time scheme, but once again converges to the classical schemes with higher resolution.

Having examined the bulk mass in outflows, it is also instructive to consider the properties of the outflow at certain heights above the disk plane. Fig. 6 shows the outflow rates (i.e. only considering outflowing gas, not inflowing), mass loading factors and mass-weighted average outflow velocity at 1 kpc and 10 kpc above the disk as a function of time for the highest two resolutions. We calculate the mass outflow as

$$\dot{M}_{\text{out}} = \frac{\sum_i m_i v_{\text{out},i}}{\Delta z}, \quad (23)$$

where the sum is over all cells within a slice (parallel to the disk plane) of thickness Δz centred on the target height (i.e. 1 or 10 kpc) that have a positive outflow velocity v_{out} (verti-

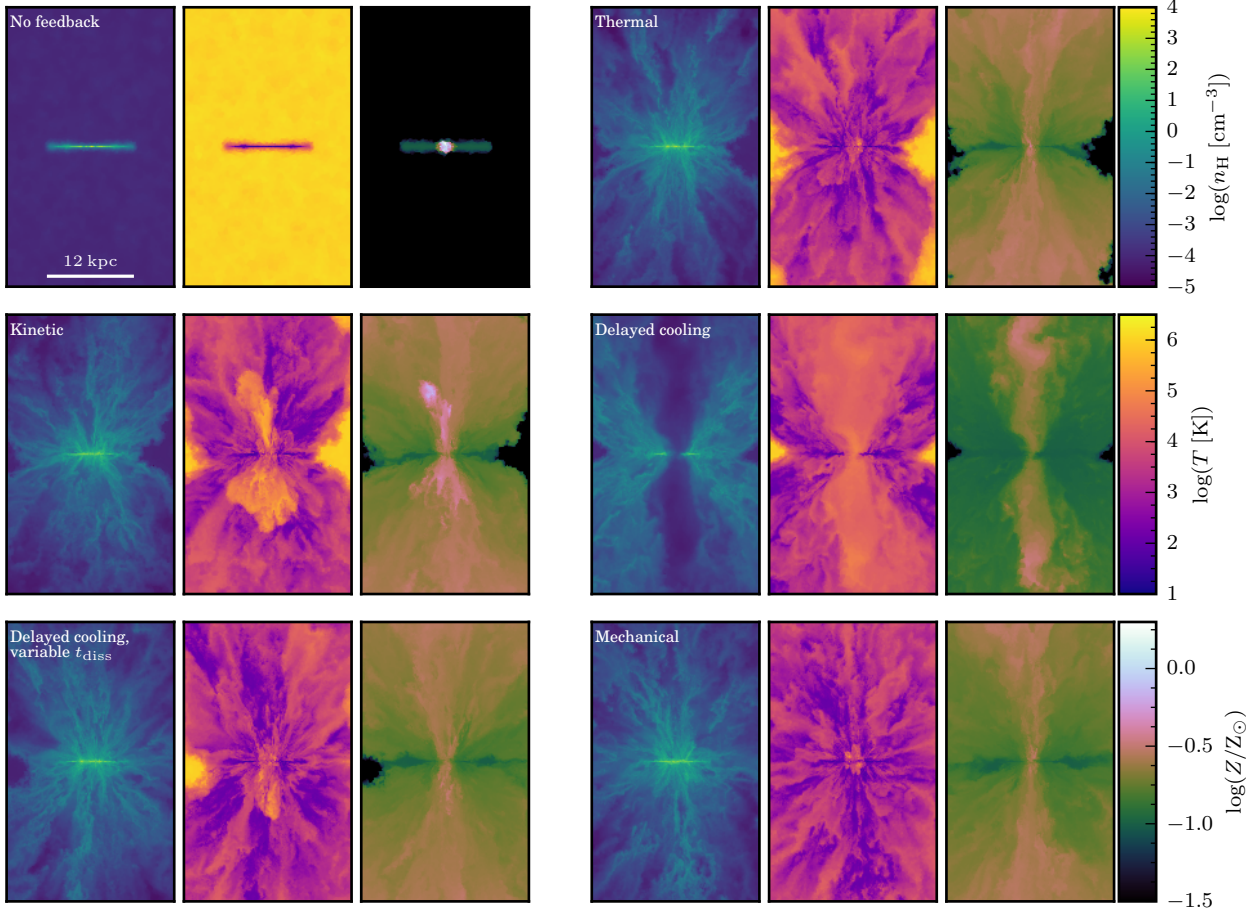


Figure 7. Density, temperature and metallicity slices at 250 Myr for $20 M_{\odot}$ resolution runs. The no feedback simulation unsurprisingly launches no outflows, leaving a high concentration of metals in the centre of the system. The classical, delayed cooling with variable t_{diss} and mechanical schemes all produce comparable outflows (differences are largely due to variability with time). The outflows have a complex filamentary structure and are multiphase with temperatures spanning ~ 6 orders of magnitude. The delayed cooling scheme evacuates gas from the centre of the system, leaving a column of very hot, low density gas. Equivalent plots for the lower resolution simulations, which are unable to launch such strong outflows, can be found in Appendix D, Fig. D3.

cally away from the disk plane, rather than radially as in the previous figures). We adopt $\Delta z = 200$ pc. The mass loading factor, β_v is the ratio of the mass outflow rate to the star formation rate and is essentially a measure of the efficiency of stellar feedback to drive outflows. There is of course a delay between the formation of a given stellar population and the outflow its feedback eventually drives reaching a given height. However, here we use the instantaneous ratio between \dot{M}_{out} and the SFR rather than a more complex binning scheme as our SFRs are, on the whole, steady over long periods (with the exception of the delayed cooling schemes, for which the mass loading must be interpreted with some caution). Finally, we plot the mass-weighted mean outflow velocity (i.e. ignoring inflowing gas) alongside the escape velocity at that height⁴.

As demonstrated in Fig. 4, with $200 M_{\odot}$ resolution, the

⁴ We calculate the escape velocity at the relevant height directly above the centre of the disk from the initial conditions. Deviations from the initial conditions during the course of the simulation have a negligible impact on v_{esc} at 1 kpc and are insignificant at 10 kpc as the dominant component is the static halo potential.

classical feedback schemes are unable to drive much of an outflow. After some initial gas flow over 1 kpc as the system settles from the initial conditions (also apparent in the no feedback simulations; this is a ‘spurious’ mass loading amplified by low SFRs), the mass outflow drops off. There is a small increase after 100 Myr as the feedback becomes more efficient and the gas reservoir is used up, but very little of this outflow reaches 10 kpc. At 1 kpc, this outflow has a mass loading factor below 0.1 i.e. significantly lower than the $\beta_v \gtrsim 1$ required by observations and models (for a more detailed discussion see introduction). The mean outflow velocities (admittedly dominated by the slower moving gas) are well below the escape velocity at 1 kpc. The mixed feedback has a higher mean outflow velocity at 10 kpc, however its seemingly increased effectiveness over the other methods can be put down to stochasticity amplified by the exceedingly small mass of gas that is actually outflowing at that distance. The mechanical feedback is able to generate a slightly more vigorous outflow, with a mass loading factor between 1 – 10 at 1 kpc. However, it is unable to sustain the outflow as previously discussed, with gas returning in a

galactic fountain. Again, very little of the outflow reaches 10 kpc.

At the higher resolution of $20 M_{\odot}$, the classical and mechanical feedback schemes are able to launch much stronger, sustained outflows. Once the outflow has reached the heights we are investigating, mass loading is around 10 at 1 kpc and over unity at 10 kpc. The mean velocities are below the escape velocity at 1 kpc, but a significant quantity of gas (see Fig. 4) is moving much faster. By 10 kpc, the slower moving gas having begun to drop back to the disk, the mean velocities are comparable to the escape velocity.

The delayed cooling simulations with fixed dissipation time are able to launch strong, but short lived outflows. Having completely quenched star formation, there is no source for additional driving of outflows beyond the initial burst. The instantaneous mass loading factor becomes an unreliable metric in such conditions, since it must naturally tend to infinity as SFR tends to zero, however we plot it here for reference. Again, using the variable dissipation time results in strong outflows at lower resolutions but similar results to the classical and mechanical feedback schemes at the highest resolution.

Fig. 7 contains vertical slices through the disk at 250 Myr for the highest resolution simulations, showing gas density, temperature and metallicity. Generating no outflows, the no feedback simulation shows a cold, thin, dense disk. The central regions have very high metallicities since the ejecta from SNe stay within the star forming regions. The thermal, mixed (not shown), kinetic, mechanical and variable dissipation time delayed cooling feedback schemes have qualitatively similar outflows. The outflows are multiphase (with temperatures in the range $\sim 10^2 - 10^7$ K) and have a complex structure, with many individual filaments apparent. Observations of galactic outflows reveal them to be comprised of multiphase gas: molecular gas at $\sim 10 - 10^3$ K observed at radio wavelengths (e.g. Walter et al. 2002, 2017; Bolatto et al. 2013), material around $\sim 10^4$ K observed in the optical and near-UV (e.g. Pettini et al. 2001; Martin et al. 2012; Soto et al. 2012) and $\sim 10^7 - 10^8$ K plasma seen in X-rays (e.g. Martin 1999; Strickland & Heckman 2007, 2009). At approximately the peak of the outflow (150 Myr), for the mechanical feedback simulation, in material moving radially outwards at more than 100 km s^{-1} , the proportions of cold (< 2000 K), warm ($2000 - 4 \times 10^5$ K) and hot ($> 4 \times 10^5$ K) material are 3.1%, 78.9% and 17.9% by mass, respectively, or 0.1%, 56.8% and 43.1% by volume. Thus, while the dominant fast moving wind component is warm, a cold component is present in the outflow. The cold component dominates by mass in material moving outwards between $5 - 100 \text{ km s}^{-1}$, with the proportions of cold, warm and hot components being 56.4%, 39% and 4.6% respectively (by volume, 0.6%, 4.2% and 95.2%, the very slow moving CGM material dominating the hot component here). As the outflow progresses and the galactic fountain effect becomes apparent, the proportions remain similar. The cold component dominates the returning gas, but warm gas also returns. It appears that the returning cold component contains both initially cold outflowing gas as well as material from the warm phase that has cooled. In summary, we find that the cold gas mainly traces the lower velocity outflows while the warm and hot medium probe the faster moving outflows; if this effect is present in real galaxies, observing

one component alone will give a biased measurement of the outflow velocity.

The results are similar for the thermal, mixed, kinetic and variable dissipation time delayed cooling feedback schemes at this resolution. Small differences between schemes apparent in the figure are largely due to stochasticity. The outflowing gas is enriched with metals and there is a dependence of metallicity on opening angle. The most metal enriched regions of the outflow are in the centre ($Z \gtrsim 0.25Z_{\odot}$), containing the highest concentration of SNe ejecta, whereas towards the edges of the outflow the metallicity is closer to the initial disk gas metallicity of $0.1Z_{\odot}$. The kinetic feedback simulation shows a high metallicity outflow of $\sim 10^6$ K gas, having had an outflow event shortly before 250 Myr. The delayed cooling with fixed dissipation time simulation exhibits a column of low density, high temperature gas that extends all the way though the centre of the disk, with cold, denser gas building up on the fringes of the outflow. At lower resolutions (see Fig. D3), the outflows are much weaker (as described above) for all simulations except the delayed cooling schemes. At $200 M_{\odot}$ resolution, the classical feedback schemes launch warm 10^4 K outflows with dense, cold edges at the interface with the CGM. The outflows are highly enriched because the mass loading is so low i.e. a substantial amount of SNe occurred to launch the outflows.

3.4 The Kennicutt-Schmidt Relation

The link between gas surface density, Σ_{gas} , and SFR surface density, Σ_{SFR} , is an important diagnostic of star formation in galaxies. Specifically, the Kennicutt-Schmidt relation, $\Sigma_{\text{SFR}} \propto \Sigma_{\text{gas}}^{1.4}$ (Kennicutt 1998), has been well established by observations of galaxies in the local Universe. Thus, in addition to suppressing absolute SFRs, it is necessary for simulations to simultaneously reproduce this relation. It is possible to have very different values of Σ_{SFR} for the same global Σ_{gas} , dependent on the small scale star formation and the degree of clustering in star formation. Our choice of small scale star formation law to some extent impacts the resulting global KS relation. For example the choice of $\dot{\rho}_* \propto \rho/t_{\text{ff}} \propto \rho^{3/2}$ generally leads to the correct slope, but this does not guarantee the correct normalization, as shown below.

Fig. 8 shows the global star formation rate surface density, Σ_{SFR} , as a function of global gas surface density, Σ_{gas} for our simulations, each point representing one of the simulations at a particular time (points are evenly spaced by 25 Myr between 25 and 250 Myr). We define the surface densities as

$$\Sigma_{\text{SFR}} = \frac{\dot{M}_*(< R_{\text{SFR},90\%})}{\pi R_{\text{SFR},90\%}^2}, \quad (24)$$

and

$$\Sigma_{\text{gas}} = \frac{M_{\text{gas}}(< R_{\text{SFR},90\%})}{\pi R_{\text{SFR},90\%}^2}, \quad (25)$$

where $R_{\text{SFR},90\%}$ is the disk radius enclosing 90% of the total

SFR⁵. For comparison, we plot global measurements from 61 normal spirals (Kennicutt 1998), similar global measurements from 19 low surface brightness galaxies (Wyder et al. 2009) and sub-kpc observations of 18 nearby galaxies (Bigiel et al. 2008). For reference, we also plot the power law fit with a slope of 1.4 from Kennicutt (1998), however it is worth noting that the slope is possibly too shallow for this range of measurements. This fit was made simultaneously to the 61 spirals plotted as well as 36 higher surface density starburst galaxies (not plotted). At lower surface densities, the relation appears to steepen, possibly due to some form of star formation threshold (e.g. Kennicutt, Robert C. 1989; Martin & Kennicutt, Jr. 2001; Bigiel et al. 2008). Thus, it makes more sense to compare our results to the data points rather than the fit plotted.

Except at the highest resolution, the no feedback and classical feedback simulations all lie well above the observed relation, although once the system has finished clumping after ~ 100 Myr, the points have approximately the correct slope. This is mainly due to the small scale star formation law adopted forcing $\dot{\rho}_* \propto \rho^{3/2}$. The simulations then progress to lower SFR and gas surface densities as the gas reservoir is consumed. At the highest resolution, the classical schemes are able to quench star formation efficiently and so drop into agreement with observations. Relative to the classical feedback schemes, the other three feedback mechanisms produce an order of magnitude lower SFR surface densities for the same gas surface density, lying close to the observed relation at all three resolutions. The delayed cooling with fixed dissipation time efficiently destroys the disk, so the majority of the snapshots lie outside the range of the plot. The same is true of the variable dissipation time run at the lower resolution, though the high resolution run is well within the observed points. The mechanical feedback runs at all resolutions agree well with the observations. The simulations track up and down the relation with time as the gas surface density changes, partly due to gas consumption, but mainly due to outflows. For example, the cluster of $20 M_\odot$ resolution mechanical feedback points (yellow squares) near the bottom left of the relation correspond to the period after the peak of the outflow at about 100 - 200 Myr, but returning gas from the galactic fountain causes the disk to have moved back up the relation by 250 Myr (open yellow square). In addition to variation over time, this effect also causes the differences between the three resolutions: the lower resolutions tend to lie higher up the relation because their weaker outflows do not drop the disk surface density as much. Despite this, the mechanical feedback points all lie close to the observations even though their exact position on the relation varies with resolution, this difference caused by the failure of resolution convergence with respect to outflows.

3.5 Host sites of star formation and supernovae

Fig. 9 shows PDFs of the local densities where stars are formed (top panels) and SNe explode (bottom panels) for our different feedback runs and at all three resolutions.

⁵ Results are fairly insensitive to the choice of the fraction of the SFR enclosed, merely sliding points up and down the Kennicutt-Schmidt relation. We only include gas within 2 kpc of the disk plane, although our results are insensitive to removing this constraint because the gas surface density is completely dominated by mass near the disk plane.

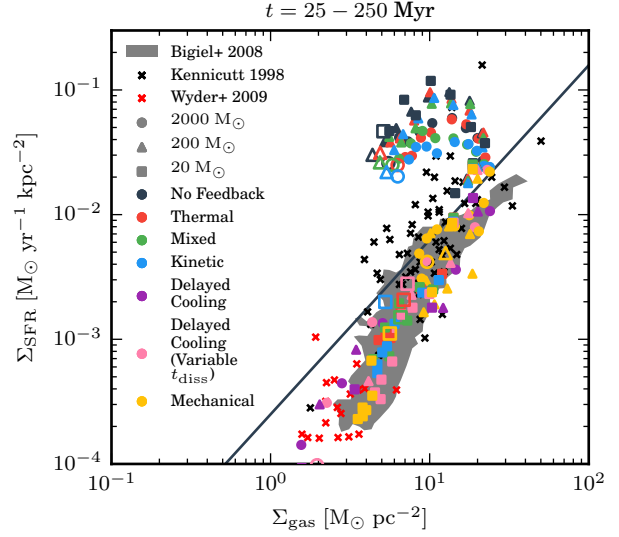


Figure 8. SFR surface density plotted as a function of gas surface density for different feedback runs at all three resolutions (as indicated by different symbols). Each symbol represents the entire galaxy at one time between 25 - 250 Myr, the open symbols corresponding to the final snapshot at 250 Myr. The black crosses are global measurements of normal spirals from Kennicutt (1998), while red crosses are similar measurements for low surface brightness galaxies from Wyder et al. (2009). The contour is derived from multiple sub-kpc measurements of 18 galaxies, including spirals and dwarfs from Bigiel et al. (2008). We plot here the contour corresponding to more than 5 data points per 0.05 dex-wide cell. For reference, we also plot the power law with a slope of 1.4 from Kennicutt (1998), fitted to both the data plotted here and higher surface density starburst galaxies. While classical feedback schemes agree with the observed Kennicutt-Schmidt relation only at the highest resolution, the mechanical feedback produces realistic SFR and gas surface densities at all three resolutions.

Looking at the sites of star formation in the simulations without feedback, a double peak form is apparent (though in the lowest resolution, the lower density peak is suppressed into more of a tail). This shape is a consequence of using a star formation threshold density (indicated by a vertical dashed line in Fig. 9). At the beginning of the simulation, as gas densities increase and cross this threshold, the first burst of star formation occurs, building a peak in the PDF just above the threshold density. The gas continues to clump until it reaches the maximum density the resolution and pressure floor allows. The majority of star formation then occurs at this density, building a high density peak in the PDF, enhanced by the fact that the SFR is higher in denser regions (i.e. $\dot{\rho}_* \propto \rho^{3/2}$). The sites where SNe occur (in this case, where mass and metals are returned but no feedback energy is deposited) are therefore an almost direct mapping from the star formation PDF because the local ISM is essentially unchanged from the star particle being born to its SNe events occurring (although continued star formation will act to drop the local density by transferring gas mass into star particles, while gas may continue to collapse to higher densities before the first SNe occur).

Inefficient feedback (i.e. the classical schemes at the lower two resolutions) follow the same behaviour as they

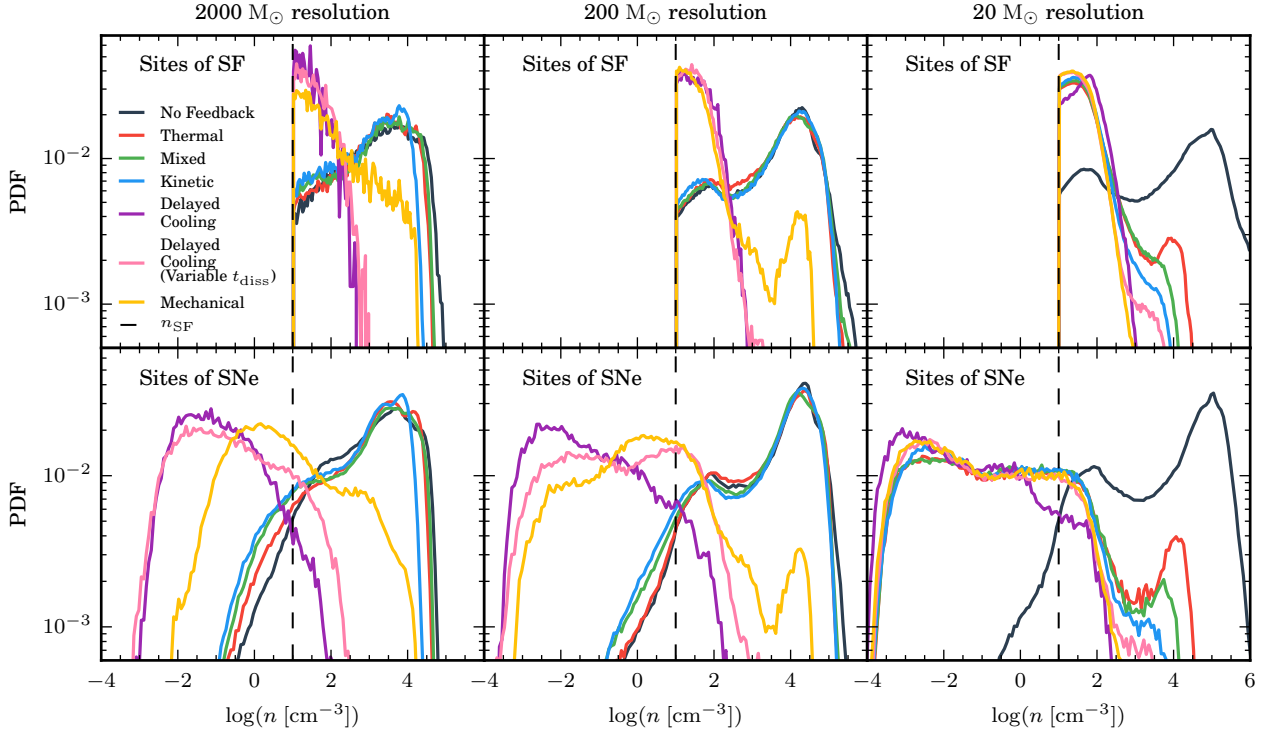


Figure 9. PDFs of the densities of the sites where stars are formed (top) and where SNe occur (bottom) throughout the entire simulation. In addition, the star formation density threshold is marked with a vertical dashed line. Without efficient feedback, the majority of stars form at high densities and SNe occur in these regions. If the feedback is able to disrupt the dense birth clouds, then subsequent SNe occur at much lower densities, leading to a tail in the PDF well below the star formation density threshold. This also prevents star forming gas from reaching such high densities.

are unable to disrupt the dense clumps of gas where the star particles are formed. In contrast, efficient feedback is able to prevent the gas from clumping to high densities, therefore increasing the fractional contribution of lower density star formation. In the case of very strong feedback that disrupts the disk (i.e. delayed cooling) the PDF of star formation is entirely dominated by the first burst of star formation, before the SNe that those star particles produce completely quench star formation. For more moderate feedback runs, the effect of a cycle of varying SFRs, caused by the return of previously ejected mass (the galactic fountain), can allow a building up of a small peak at high density. For example, in the 200 M_{\odot} resolution mechanical feedback run, after a period of low SFR between 50 and 200 Myr (see Fig. 3), the small peak at $\sim 10^4 \text{ cm}^{-3}$ is able to form before the feedback is able to start destroying clumps again. The degree to which this effect occurs is an indication of how effective a given feedback scheme is at dispersing dense gas at a low local SNe rate, since this is directly linked to the local SFR (with an offset arising from a delay between massive star formation and SNe occurrence). In other words, once the SFR has been reduced by feedback, if the resulting lower SNe rate is unable to efficiently prevent the return of gas, a high density peak in the SF PDF will occur. Specifically, in the highest resolution simulations, the thermal feedback shows a small peak at $\sim 10^4 \text{ cm}^{-3}$ while the mechanical feedback does not (with mixed, kinetic and delayed cooling with variable dissipation time lying between the two in or-

der of their effectiveness). Note that the shape of the PDF above the star formation threshold will also be dependent upon the details of the small scale star formation prescription adopted; this is discussed in Section 3.8.

With efficient feedback, the shape of the PDF of densities of SNe sites above the star formation threshold corresponds closely to the star formation PDFs, as in the inefficient feedback case. However, the PDF extends well below the star formation density threshold. Since by definition the star particles from which the SNe are occurring cannot have been formed at these densities, these SNe are occurring after previous SNe have disrupted the star forming regions of their birth cloud.⁶ Of course, more efficient feedback results in more SNe occurring in low density environments. These subsequent SNe are themselves more efficient because momentum input into the ISM is higher at lower ambient densities (but also numerically, in the case of the classical schemes, because it is easier to resolve the Sedov-Taylor phase). Thus, particularly when other faster acting stellar feedback effects

⁶ An alternative mechanism by which SNe can occur outside of dense star forming regions requires the SNe progenitors to have moved out of their birth clouds (i.e. OB runaways, see e.g. Conroy & Kratter 2012), most likely as a result of interactions with other stars. Because we do not resolve the dynamics of individual stars in their clusters, this effect is not present in our simulations. We could adopt an additional sub-grid recipe to replicate this (e.g. Ceverino & Klypin 2009; Kimm & Cen 2014; Kim & Ostriker 2016), but this is beyond the scope of this work.

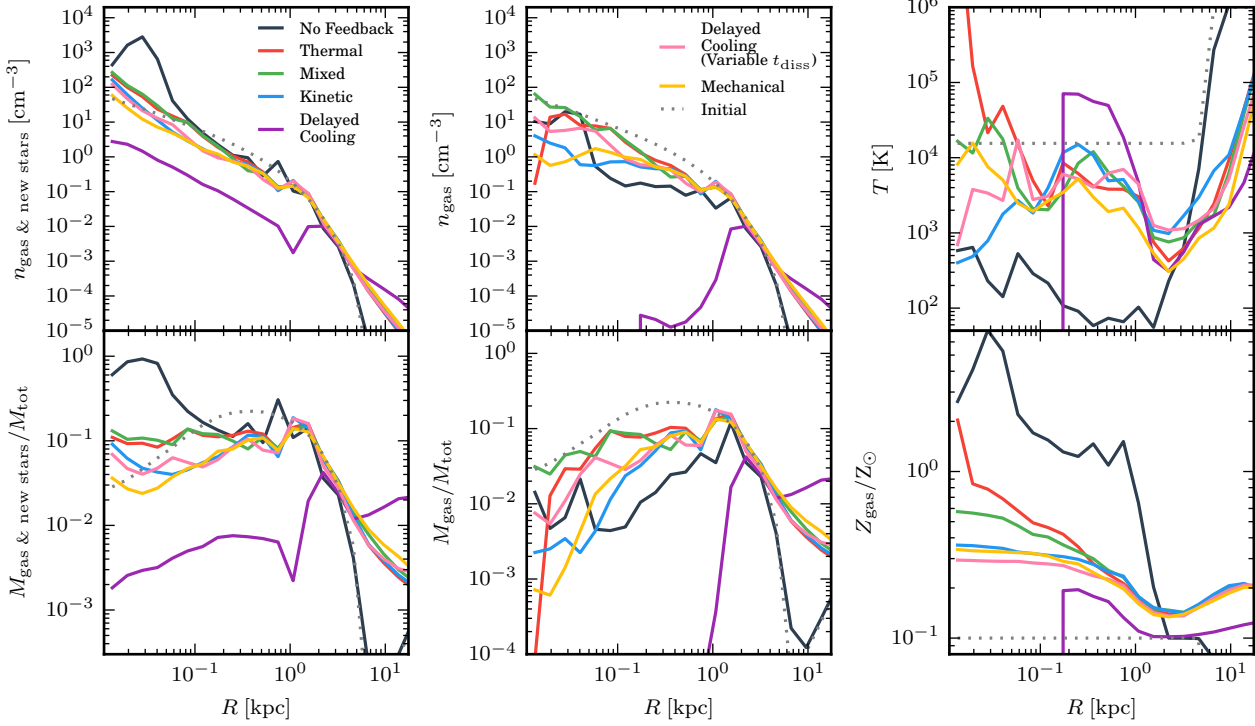


Figure 10. Spherically averaged radial profiles of number density of gas and newly formed stars, gas number density, gas temperature (top panels) and mass fraction of gas and newly formed stars, gas mass fraction and gas metallicity (bottom panels) for our different feedback runs at 250 Myr for simulations with $20 M_{\odot}$ resolution. The profiles from the initial conditions are shown with gray dotted curves.

are not included (as in our work), a major requirement of an efficient SNe feedback scheme is that the first SNe to occur in a star forming region are able to disperse the dense gas to allow the efficiency of later SNe to be increased. The classical feedback schemes are only able to achieve this at the highest resolution probed. The mechanical feedback scheme is more successful at all resolutions, but with increasing resolution more SNe go off in lower density environments. At the highest resolution, the shape of the PDF below the star formation density threshold is similar for all feedback schemes. Because the delayed cooling schemes result in a rapid clearing of gas from the centre of the system, most SNe occur in low density gas at all resolutions.

3.6 Structure and kinematics

Fig. 10 shows the spherically averaged radial profiles of number density and mass fraction of gas together with new stars, and of gas separately, as well as mass-weighted gas temperature and metallicity, for the highest resolution simulations at 250 Myr. The profiles from the initial conditions are also plotted for comparison. The no feedback shows an enhancement in baryon number density and mass fraction, due to a large centrally positioned clump (see Fig. 1). A smaller peak caused by another clump further out is also apparent. However, the density and mass fraction of the gas component taken on its own are significantly reduced from the initial conditions, indicative of a major conversion of gas to stars in situ. The profiles are unchanged at large radii as there

has been no outflow of material. The temperature within the disk gas has dropped by several orders of magnitude due to metal cooling. The metallicity of disk gas has increased by a factor of 10 – 100 because of the high SFR in conjunction with the lack of outflows, resulting in very short cooling times.

The classical, mechanical and delayed cooling with variable dissipation time feedback schemes are similar to the initial conditions with respect to the baryon number density and mass fraction in the central regions. The gas mass fraction has been reduced, as have the central densities, partly due to conversion of gas to stars (as in the no feedback case) but mainly due to outflowing material. This outflow material can be seen at larger radii, where the gas mass fraction outside ~ 4 kpc has been significantly increased. The gas within the disk has been prevented from runaway cooling and the average temperature within the is mostly between $10^3 - 10^4$ K. Variations in temperature between the different feedback schemes are largely transient and stochastic, particularly at small radii (where the average is over less gas mass). Temperatures are significantly reduced from the initial conditions outside a few kpc, as colder outflowing gas displaces the hot CGM. Central metallicities are increased from the initial conditions by a factor of $\sim 3-8$ (with the exception of a metallicity spike from the recent feedback event in the thermal simulation which has not yet dispersed). Metals have been transported into the region initially occupied by the CGM. As previously described, the delayed cooling with fixed dissipation time evacuates gas from the central

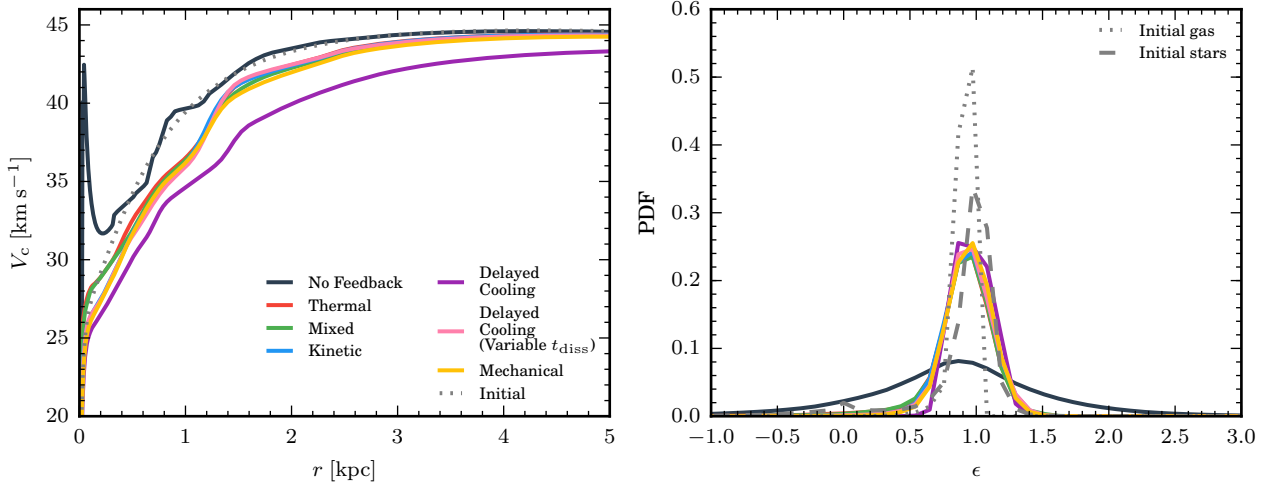


Figure 11. Circular velocity profiles (left) and circularities, $\epsilon = j_z/j_c$, (right) for newly formed stars at 250 Myr for our different feedback simulations at $20 M_\odot$ resolution. We also plot the initial circular velocity profile (left) and distribution of circularities for stars present in the initial conditions and of gas (within 3 scale radii and 3 scale heights) (right). The circular velocity profiles are largely unchanged from the initial conditions (due to the largely unchanged initial stellar disk and the static halo potential). The no feedback simulation is peaked close to the centre due to presence of a clump of gas and stars. The simulations with feedback reduce the circular velocity slightly by transporting mass outwards. All simulations have circularity distributions centred at ~ 1 , indicative of a disk. There is no signature of a bulge component. The no feedback simulation has a broader distribution of circularities due to the highly clumped disk structure.

regions extremely efficiently, resulting in a large drop in the central gas density and mass fraction, a spike in temperature of the remaining gas but a very small increase in metallicity (because there have been very few SNe). Despite the explosive nature of delayed cooling feedback, the mass-averaged temperature at the outer radii (1 – 10 kpc) is still much lower than the original CGM temperature. The lower resolution simulations (not shown) have very similar profiles to those described above, dependent on whether how effective the feedback is (i.e. the classical schemes overcool so adopt the same behaviour as the no feedback case). We have also examined surface density profiles (not shown) and find that the results are similar to the radial profiles. Simulations with feedback preserve the initial exponential density profile of the disk in terms of total baryons. The gas profiles are centrally cored relative to the initial profile and densities are enhanced at outer radii due to outflows.

Fig. 11 shows the circular velocity profiles and distribution of circularity parameter, $\epsilon = j_z/j_{\text{circ}}$, for newly formed stars for our different feedback runs at the highest resolution. The circular velocities are generally similar to initial conditions, because the distribution of the initial stellar disk and (small) bulge of old stars is largely unchanged (these components making up over half of the initial baryonic mass), while at larger radii the circular velocity is dominated by the static halo potential. The no feedback case shows a peak at small radii due to the centrally positioned clump remarked upon earlier. Note, as described above, this clump cannot be taken to be indicative of bulge formation. As seen in Fig. 1, there are multiple clumps present in the disk. The position of the clump is somewhat stochastic. We have found other simulations at a variety of resolutions to produce the same degree of clumping, yet not necessarily with a clump positioned close enough to the centre to produce a central peak in the circular velocity profile. However, as seen in Fig. 11,

efficient feedback results in a reduction in circular velocity, particularly at small radii, due to the transport of gas mass out to further radii.

The circularity parameter gives an indication of the degree of rotational support in a system by comparing the specific angular momentum in the z -direction (i.e. out of the disk plane) to that required for a circular orbit at the same radius. Thus, stars belonging to a disk will have $\epsilon \sim 1$, whereas a non-rotating spheroid would have a symmetric distribution about $\epsilon = 0$. All simulations have a peak around $\epsilon \sim 1$, indicative that the newly formed stars form a disk, while there is no clear signature of a bulge component (such as the small enhancement at $\epsilon = 0$ present in the initial stars). This is not surprising because the stars have formed directly from the gas disk. The distribution is peaked very slightly below $\epsilon = 1$; this is inherited from the initial gas distribution which has some degree of pressure support in addition to the rotational support (as can be seen by comparing the initial distribution of gas circularities to those of the stellar disk). The difference between no feedback and feedback simulations is apparent in the width of the distribution. With feedback, the stellar circularities are relatively narrowly distributed around 1 (irrespective of the feedback scheme adopted), whereas in the no feedback gas the distribution is considerably broader. This is caused by the highly clumpy disk formed in this run, with stars acquiring significant offsets from the circular velocity due to local interactions with clumps.

We conclude this section by remarking that a proper study into the effects of the feedback schemes on galaxy structure and kinematics should make use of galaxies formed self-consistently in a cosmological context, rather than in a disk set up ‘by hand’ as in this work. However, we find it informative to examine the extent to which an ideal system is maintained in the presence of our feedback schemes, rang-

ing from a strongly clumped distribution in the no feedback case to total disk destruction due to overstrong feedback in the delayed cooling case.

3.7 Varying galaxy mass

In addition to our fiducial $10^{10} M_{\odot}$ galaxy, we have also run simulations of smaller ($10^9 M_{\odot}$) and larger ($10^{11} M_{\odot}$) systems without feedback and with mechanical feedback at our intermediate resolution of $200 M_{\odot}$. The results of these simulations are summarised in Fig. 12 alongside the equivalent simulations of our fiducial system, showing mass of newly formed stars (expressed as a fraction of the initial disk gas budget), specific star formation rates (SSFR) and mass loading factors at two distances from the midplane of the disk. For a comparison between the systems, the mass loading is measured across planes the same distance away from the centre scaled by the virial radius of the systems. For our fiducial galaxy mass this is 1 kpc and 10 kpc, so we use 0.47 kpc and 4.7 kpc for the smaller system⁷ and 2.16 kpc and 21.6 kpc for the larger system.

In the smaller system, the simulation without feedback quickly starts forming stars from the beginning of the simulation, though it quickly establishes a steady SSFR of $\sim 2 \times 10^{-10} \text{ yr}^{-1}$ as the smaller surface densities prevent gas from clumping to high densities. This SSFR is approximately an order of magnitude smaller than the fiducial simulation. The mechanical feedback initially follows the same evolution as the no feedback case. However, once the SFR has reached its peak, the SNe are able to unbind the gas from system due to the shallow potential well, quenching star formation. At 250 Myr, the ratio of newly formed stellar mass to the initial gas disk mass is approximately an order of magnitude lower than the fiducial simulation. This trend agrees with the general results from abundance matching that lower mass galaxies are less efficient at forming stars (below $\sim 10^{12} M_{\odot}$) (see e.g. Moster et al. 2013; Behroozi et al. 2013). However, the factor by which feedback has suppressed star formation relative to the no feedback simulation is similar to the fiducial case. This suggests that the lower star formation efficiency relative to the fiducial simulation is inherent to our particular setup, rather than being caused by more efficient feedback as is commonly posited to explain the phenomenon. After the spuriously high mass loading due to the low SFR at the beginning of the simulation has reduced (note that the no feedback simulation continues to have a relatively high apparent mass loading for the same reason), the mass loading at 0.47 kpc and 4.6 kpc rises dramatically as the gas is expelled from the system. The mass loading then tends to infinity because the SFR has dropped to zero (the instantaneous mass loading factor is not a good metric in a highly bursty regime).

Without feedback, the larger system follows an evolution similar to that of the fiducial system. However, it forms stars more than proportionally faster than the fiducial case, resulting in ~ 3 times more stellar mass formed than a simple scaling with the system mass. With mechanical feedback, the result is similar relatively speaking, with star formation suppressed by a similar factor. Once again, the trend of a greater star formation efficiency seems to be qualitatively in line with abundance matching, but, as with the low mass

⁷ We use a thickness $\Delta z = 100$ pc for determining the mass outflow rates for the smaller mass system.

system, this effect seems to be inherent to the set-up rather than caused by less efficient feedback. The mass loading factor is mostly within a factor of a few of the fiducial simulation at both distances, though is always lower. The mass loading factor is mostly below unity at 2.16 kpc and reaches a maximum of only 0.1 at 21.6 kpc, i.e. the outflows are even more inefficient than in our fiducial galaxy model, which is not unsurprising given the deeper potential well outflows need to overcome.

3.8 Varying star formation law parameters

While the focus of this work is on the difference between different feedback schemes, we also briefly examine here the effect of varying the parameters used with our adopted star formation law (see equation (2)). We rerun our $200 M_{\odot}$ resolution simulations of the fiducial galaxy without feedback and with mechanical feedback but with an increased star formation efficiency parameter, $\epsilon_{\text{SF}} = 15\%$ rather than the fiducial 1.5% and also with an order of magnitude higher density threshold, $n_{\text{SF}} = 100 \text{ cm}^{-3}$. The results are summarised in Fig. 13 alongside the fiducial simulations.

Increasing the star formation efficiency parameter by an order of magnitude results in the initial SFR being an order of magnitude higher than the fiducial case both with and without feedback. The simulation without feedback maintains this high SFR ($\sim 1 M_{\odot} \text{ yr}^{-1}$), dipping slightly below the fiducial simulation's SFR, which has risen to this value, at ~ 110 Myr as the gas reservoir is consumed. The final newly formed stellar mass is approximately 1.25 times larger than the fiducial run. In the mechanical feedback case, the high SFR leads to a burst of strong feedback at 20 Myr which expels the gas from the centre of the system and quenches star formation. The mass in newly formed stars at 250 Myr is similar to the fiducial simulation, but the majority of stars have formed in the first 50 Myr. Once again, the instantaneous mass loading factor for a regime that quenches star formation is an unreliable metric (as it tends to infinity as the SFR plummets). However, there is a brief period between 20 – 100 Myr where the SFR is non-zero, leading to a mass loading factor between 1 – 50 at 1 kpc. The outflow also easily reaches the 10 kpc plane as can be seen by the high mass loading factor.

Increasing the star formation density threshold by an order of magnitude results in an initially lower SFR in the simulation without feedback as it takes slightly longer for the gas to reach the higher star forming densities. However, by 70 Myr, the SFR has reached the levels of the fiducial simulation and subsequent evolution is similar, resulting in the almost the same mass in new stars at 250 Myr. The simulation with mechanical feedback is similar until 50 Myr, when the SNe are able to halt further rising of the SFR. A stable SFR is established, a factor of a few higher than the fiducial simulation. The stellar mass at 250 Myr is only 1.4 times that of the fiducial simulation. The outflow is weaker at 1 kpc by a factor of a few than the fiducial case for most of the simulation, stable at around unity. However, at 10 kpc the outflow is very weak, with mass loading factor between $10^{-3} - 10^{-2}$ (an order of magnitude lower than the fiducial simulation).

Fig. 14 shows PDFs of the gas densities at the sites of star formation and SNe explosions, comparing the models with altered star formation law parameters to the fiducial

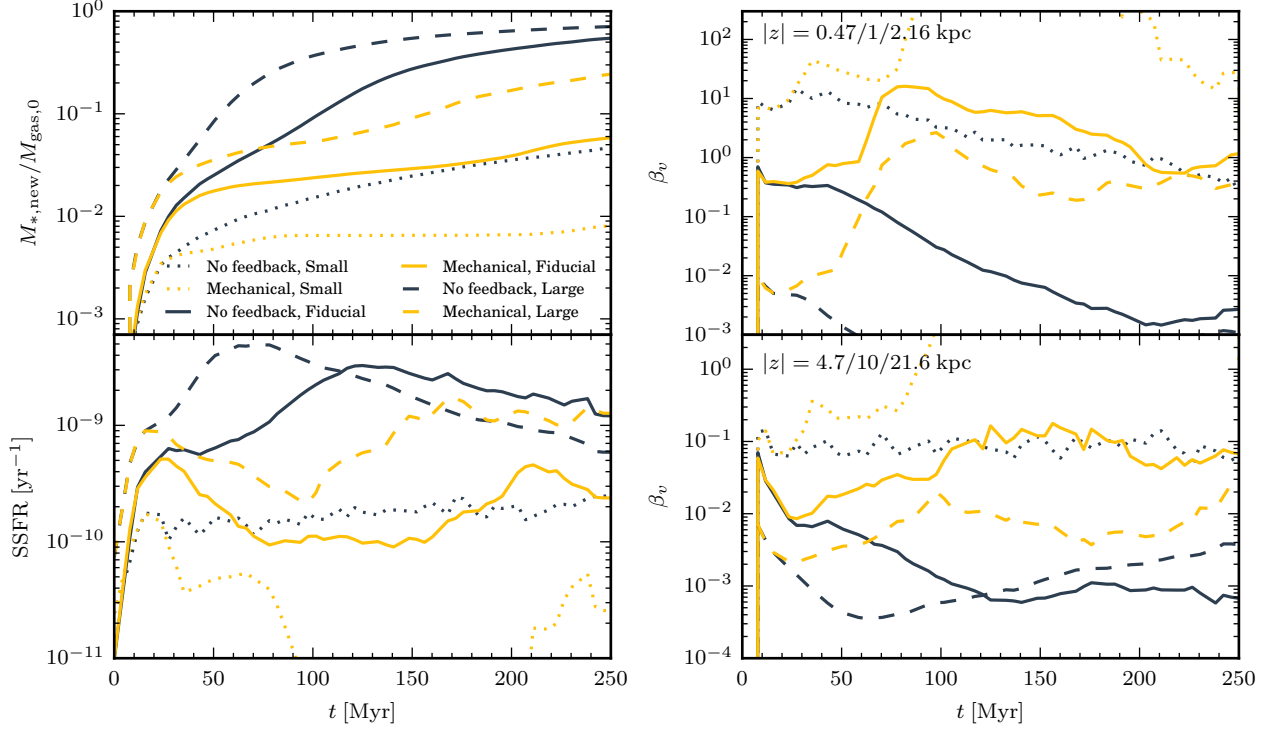


Figure 12. A comparison of simulations with no feedback and with mechanical feedback for our three galaxy masses (see Table 1) at $200 M_{\odot}$ resolution. *Top left:* Newly formed stellar mass expressed as a fraction of the initial gas disk mass. *Bottom left:* specific star formation rates (\dot{M}_*/M_* where M_* includes both old and new stellar mass). *Right:* mass loading factor across two planes at different distances from the disk midplane. For the fiducial galaxy, these are 1 and 10 kpc as in Fig. 6. For the small and large galaxies, the planes are at the same distance relative to the virial radius as in the fiducial case (0.47 and 4.7, 2.16 and 21.6 kpc, respectively). Global star formation efficiency increases with increasing system mass (a trend in line with abundance matching), though this appears to be independent of feedback in our setup. Feedback suppresses star formation by a similar factor in all three systems. Outflows become weaker with increasing system mass.

simulation. The simulation with increased star formation efficiency produces most of its stars in gas that is several orders of magnitude less dense than the fiducial case, because gas is rapidly converted to stars before it can collapse to higher densities. This means that SNe occur in lower density gas, enhancing their momentum input into the ISM. This, coupled with the increased SNe rate relative to the fiducial run gives rise to the quenching of star formation and the generation of stronger outflows.

In the simulations with a higher star formation threshold density, without feedback, the PDFs of star formation and SNe site densities are similar, because most star formation occurs in gas at $n = 10^4 \text{ cm}^{-3}$, well above the thresholds. However, in the runs with mechanical feedback, the situation is different. In the fiducial simulation, feedback shifts the peak star formation density down to the threshold. In the simulation with a higher threshold density, stars are born at much higher densities. The result is that SNe occur in gas of higher density which reduces their momentum input to the ISM. The feedback is still strong enough to disrupt star forming regions, which is why the SFR is close to the fiducial case, but the reduction in momentum results in weaker outflows. Note that the reduction in momentum input is not due to overcooling, but is physical (see equation (22)), although the subsequent development of outflows is subject to resolution effects, as discussed in Section 3.3.

What we have demonstrated in this section is that changing the star formation prescription (to not unreasonable values) can have a non-negligible effect on SFR and outflows, although a more comprehensive study of these effects is beyond the scope of this work. We note that a low mass system such as our fiducial model is likely to be less robust to changes in the star formation prescription because it is easy to unbind gas if the feedback increases in strength, leaving little margin for self-regulation, although we find our results to be broadly in agreement with similar tests in Rosdahl et al. (2017). It is also likely that the inclusion of other feedback processes that act in the time between star formation and the resulting SNe might possibly help mitigate the dependence on the star formation prescription by preventing further collapse of gas (see Hopkins et al. (2011, 2013) for examples of self-regulating systems that are somewhat robust to the star formation prescription in terms of the global SFR).

4 DISCUSSION

4.1 Comparison of SN feedback implementations

We find that our ‘classical’ schemes (simple injection of thermal energy, kinetic energy or a mixture of the two) all give very similar results. There is a slight trend for an injection

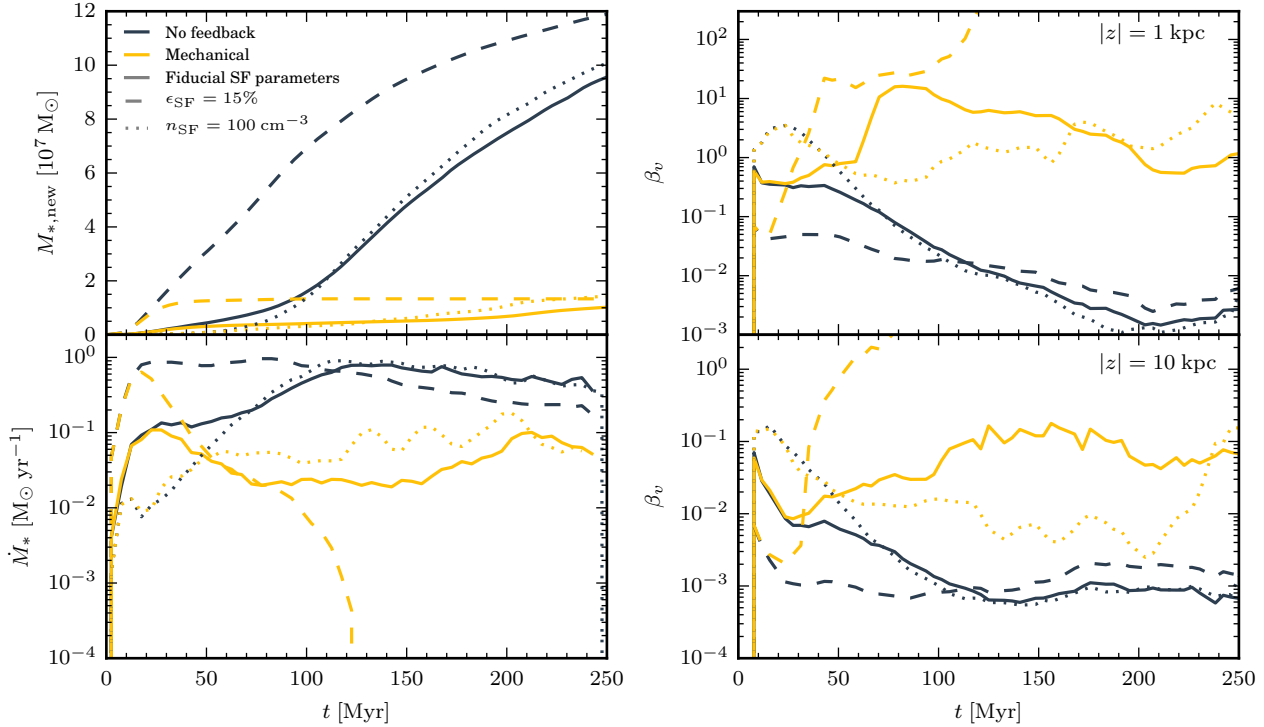


Figure 13. Simulations with no feedback and mechanical feedback with varying star formation criteria at $200 M_{\odot}$ resolution for our fiducial galaxy. We compare our fiducial values for star formation ($\epsilon_{\text{SF}} = 1.5\%$, $n_{\text{SF}} = 10 \text{ cm}^{-3}$) with an increased star formation efficiency ($\epsilon_{\text{SF}} = 15\%$) or an increased star formation threshold density ($n_{\text{SF}} = 100 \text{ cm}^{-3}$). *Top left:* Newly formed stellar mass. *Bottom left:* SFRs. *Right:* mass loading factor across two planes at different distances from the disk midplane. These are at 1 kpc and 10 kpc as in Fig. 6. Increasing ϵ_{SF} results in faster star formation, leading to a much stronger burst of feedback which quenches subsequent star formation. Increasing n_{SF} results in a similar evolution of stellar mass to the fiducial case, but produces weaker outflows.

of kinetic energy to result in stronger feedback but the effect is minor. At all but the highest resolution of $20 M_{\odot}$ these schemes suffer from the overcooling problem, barely suppressing star formation relative to the no feedback case and producing similar clumpy morphologies. This is not unexpected.

One can alleviate the problem slightly by injecting the energy of several SNe at once, but only up to a point. For example, Rosdahl et al. (2017) inject the energy of 40 SN simultaneously which allows a thermal dump to be efficient in their $10^{11} M_{\odot}$ system but not in their $10^{12} M_{\odot}$ system, due to a combination of the deeper potential, stronger metal line cooling, higher densities and lower resolution. In addition, such an approach requires the adoption of an artificial delay time between the birth of a star particle and the triggering of a SN event. Kimm et al. (2015) find that allowing for a realistic delay time, with individual SNe distributed between $\sim 3 - 40$ Myr, prevents the build up of dense gas prior to SNe occurring relative to a fixed delay time of 10 Myr, while also allowing later SNe to explode in low density environments produced by earlier events. The caveat, of course, is that individual SNe are more susceptible to overcooling.

Our trial of delayed cooling schemes is unsatisfactory. Unlike the other schemes explored, these schemes have adjustable parameters, which is something we wish to avoid if possible. In addition, delayed cooling schemes circumvent unphysical results caused by lack of resolution by enforcing

an equally unphysical adiabatic phase on large scales. The scheme with a fixed dissipation time of 10 Myr produces far too violent feedback at all resolutions, completely destroying the disk and giving rise to an unphysical pattern of star formation as gas is ejected from the system. This suggests our choice of parameters is incorrect, though we test a higher effective velocity dispersion threshold (100 km s^{-1} instead of our fiducial 10 km s^{-1}) without a drastic change in results (see Appendix C) and also note that our choice of parameters is not wildly different from others used in the literature at similar resolutions (see e.g. Teyssier et al. 2013; Rosdahl et al. 2017, though Dubois et al. 2015 determine lower values for the dissipation time). Our attempts to modulate the dissipation time with resolution ($t_{\text{diss}} = \Delta x / \sigma_{\text{FB}}$), suggested in Teyssier et al. (2013) as an alternative parametrization, do not converge with resolution, being similar to the fixed dissipation time at low resolution while essentially acting as a simple thermal dump at high resolution. No doubt both these schemes could be improved were we to spend more time tuning the parameters, but this would not achieve our goal of finding a physically motivated model ideally free from adjustable parameters. We also note the concerns of Rosdahl et al. (2017) that their delayed cooling scheme trialled does not converge with their thermal dump when the adiabatic phase is resolved (as we find), suggesting that the scheme does not necessarily converge to the correct answer.

The most successful scheme explored is the mechani-

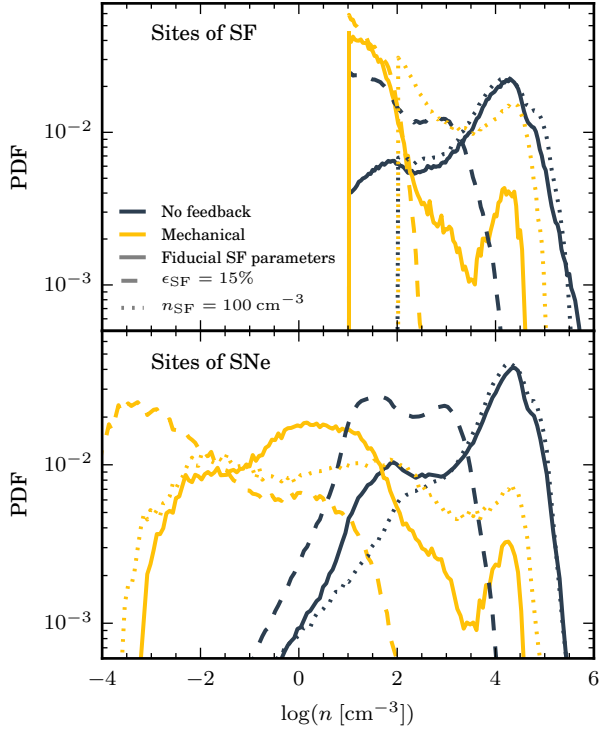


Figure 14. PDFs of the densities of the sites where stars are formed (top) and where SNe occur (bottom) for the simulations in Fig. 13, comparing the effects of changing the star formation law parameters using our fiducial galaxy mass and $200 M_{\odot}$ resolution. Increasing ϵ_{SF} results in gas being rapidly converted to stars before it can reach high densities. A strong burst of initial feedback disrupts star forming clouds, so the majority of SNe occur at very low densities. Increasing n_{SF} has very little impact on the PDFs, though slightly more SNe occur at high densities.

cal feedback scheme. It suppresses star formation by similar factors across two orders of magnitude in mass resolution (though is slightly stronger at higher resolution), prevents the formation of highly dense clumps of gas, preserves the disk structure and agrees with observations of the Kennicutt-Schmidt relation (though the exact position on the relation has a resolution dependence caused by non-convergent outflow properties, discussed below). It also gives similar results to the classical schemes at the highest resolution, suggesting it is converging onto the correct answer. This latter feature was also noted in Rosdahl et al. (2017) and demonstrates that the ability of the scheme to converge on the final momentum input to the ISM per SN (as shown in Kimm & Cen 2014) translates into convergent behaviour for global properties. The mechanical feedback is slightly stronger than the classical feedback schemes because, even at this resolution, they are likely to still experience some overcooling at the highest density SN sites. The one area where the mechanical scheme does not converge is in outflows, which we discuss next.

4.2 Difficulties in outflow generation and the possible effects of missing physics

Having concluded in the previous section that the mechanical feedback scheme is the best amongst those explored,

we choose to focus on it for this discussion. At the highest resolution, the scheme produces well developed multiphase outflows with appropriate mass loadings compared to observations and theory ($\beta_v \approx 1 - 10$), which is very encouraging (similar results are obtained by the classical schemes and the variable t_{diss} delayed cooling at this resolution). What is not so encouraging, however, is that the outflows are considerably weaker at a mass resolution of $200 M_{\odot}$ and practically non-existent with $2000 M_{\odot}$, despite similar results with other galaxy properties. This also has the effect of moving the disks up the Kennicutt-Schmidt relation with decreasing resolution because the disk surface density is increased (though it should be noticed that these still match observations). Rosdahl et al. (2017) also report difficulties in driving outflows with mechanical feedback with a resolution similar to our lower resolutions simulations.

Such inefficient outflows could be caused by an oversimplified model of SN expansion. The mechanical feedback scheme treats the unresolved evolution of the SN remnant as expanding through a uniform medium. In reality, the ISM is likely to be porous due to a turbulent structure, containing low density channels through which gas accelerated by the SN can escape, leading to higher velocities. Haid et al. (2016) model this effect by considering the ISM surrounding the SN as a set of cones of different densities (randomly drawn from a log-normal distribution appropriate for the level of turbulence assumed) and use the results for a uniform medium within each cone. They find that momentum can be boosted by up to a factor of 2 in a low density environment. Our scheme already approximates this approach because it calculates the boost factor for each neighbour cell independently, a point that is argued by Hopkins et al. (2018). However, we would caution that this assumes that the turbulent structure of the ISM is well resolved in the simulation, which is very unlikely to be the case, and will introduce a resolution dependence. However, the momentum boost measured in Haid et al. (2016) is weak; similar results are found in other studies with full 3D simulations (e.g. Iffrig & Hennebelle 2015; Martizzi et al. 2015; Kim & Ostriker 2015; Li 2015; Walch & Naab 2015), some of which find a slight negative impact on final momentum input versus the uniform case. However, while the final momentum input into the ISM may be only weakly effected by a turbulent medium, the amount of mass involved in the expansion and therefore the wind velocities reached can be altered. Kimm et al. (2015) trial a modification of their version of mechanical feedback in AMR simulations where they reduce the mass entrained from the host cell to 10% to replicate this effect, resulting in a greater suppression of star formation and higher mass loading factors. They state, however, that this fraction was somewhat arbitrarily chosen. Unless a physically motivated method of determining the fraction to be entrained based on unresolved structure was used, this could easily become just another tunable parameter. A final problem is that with a constant mass, as by definition imposed with a Lagrangian code, there is a minimum mass that can be momentum boosted. Even if we inject the correct momentum, the effects can be diluted if it is injected into too much mass resulting in lower velocity winds, effectively imposing a minimum resolution requirement.

Another potential cause of inefficient outflows experienced here could be the lack of other stellar feedback mech-

anisms. In particular, the ability of other feedback mechanisms to disrupt GMCs will enhance subsequent SN feedback. An obvious mechanism is that of photoionisation (see e.g. Vázquez-Semadeni et al. 2010; Walch et al. 2012; Dale et al. 2014; Sales et al. 2014). Geen et al. (2015) found that the final momentum input to the ISM by SN is increased when the surrounding medium has been preprocessed by photoionisation feedback by forming an over-pressurised and lower density region in which the SN occurs. Kimm et al. (2017) modify their mechanical feedback prescription to include this momentum boost when they under-resolve the Strömgren sphere in their RHD simulations. Hopkins et al. (2012a, 2014) find that if they turn off radiative feedback (radiation pressure, photoionisation and photoelectric heating), outflow mass loadings are reduced because GMCs are no longer efficiently disrupted prior to SN occurring (though the strength of the effect is dependent on the mass of the system). Simulating an isolated system similar to our fiducial model, Hu et al. (2017) find that while SNe are the dominant feedback mechanism, the inclusion of photoionisation increases outflow rates by reducing the ambient density at SN sites. However, in their simulations, the inclusion of photoelectric heating reduces outflows because it reduces the SFR and therefore the number of SN occurring, while being unable to drive outflows itself.

As noted in Section 3.8, the choice of star formation prescription can also impact the effectiveness of feedback. We found that increasing the star formation efficiency parameter by a factor of 10 led to stronger outflows (and the destruction of the disk) because the SFR was initially higher and gas could not reach high densities before SN occurred, leading to a sudden, strong burst of efficient feedback. Instead, increasing the threshold density had only a marginal impact on the SFR, but produced weaker outflows because SN occurred in slightly denser environments. The adoption of other feedback mechanisms would probably mitigate this effect. It is also worth noting that we have only tested changes of parameters to our simple star formation prescription. More complex prescriptions may rely on the selection criteria of star forming gas rather than an efficiency parameter (see e.g. Hopkins et al. 2013, 2014, and subsequent papers, which use an efficiency of 100%, but require gas to be self-gravitating, self-shielding and very dense). Alternatively, it has been suggested that while the globally averaged star formation efficiency may be on the order of a few percent, small scale efficiencies vary based on the local properties of the ISM (see e.g. Krumholz & McKee 2005; Padoan & Nordlund 2011; Hennebelle & Chabrier 2011; Federrath & Klessen 2012). In line with this, a star formation prescription could adopt a variable efficiency (see e.g. Kimm et al. 2017). Such schemes are likely to impact the distribution of gas densities by allowing high density non-star forming gas to exist, as well as impacting SN feedback effectiveness by altering the clustering properties of stars in both space and time.

5 CONCLUSION

Using an isolated disk galaxy setup and a new implementation of star formation and SN feedback in the moving mesh code AREPO, we tested several SN feedback prescriptions commonly found in the literature and assessed their impacts on a variety of galaxy metrics, paying particular attention to how well they converge as a function of resolution. The bulk

of our simulations were of a $10^{10} M_{\odot}$ system, although simulations were carried out of systems an order of magnitude lower and higher in mass. In order to test the convergent properties of the feedback schemes with resolution, simulations were carried out with resolutions of $2000 M_{\odot}$, $200 M_{\odot}$ and $20 M_{\odot}$. The schemes tested were designed to be used in isolated galaxy or cosmological zoom-in simulations, using individually time resolved SN events. Specifically, we investigated ‘classical’ dumps of thermal and/or kinetic energy, two parametrizations of delayed cooling and a mechanical feedback scheme which injects the correct amount of momentum relative to the stage of the SN remnant evolution resolved.

Without feedback, our simulations produce a highly clumpy disk and overproduce the mass of newly formed stars. As expected, the ‘classical’ feedback schemes overcool at all but the highest resolution. The delayed cooling schemes tested are far too strong, unphysically destroying the disk. We note that we could tune these simulations more carefully to avoid this effect, but because we wish to avoid adjustable parameters as much as possible we do not consider these schemes to be suitable for our purpose. Our mechanical scheme is the best tested, suppressing star formation by similar factors at all three resolutions, preventing the formation of highly dense clumps of gas, agreeing with observations of the Kennicutt-Schmidt relation while also preserving the disk structure. It also produces similar results to the ‘classical’ schemes at $20 M_{\odot}$ resolution, suggesting it is converging onto the physically correct results.

At the highest resolution our mechanical scheme produces multiphase outflows with reasonable mass loading factors relative to observations and theory ($\beta_v \approx 1 - 10$), as do the ‘classical’ schemes at the highest resolution. However, we struggle to produce outflows at lower resolution. This may be due to an oversimplification of the way in which we model SN remnant evolution, for example failing to adequately account for the unresolved porous structure of the ISM. The situation may also be improved by the inclusion of other forms of stellar feedback that are able to preprocess the ISM and enhance the ability of the SN feedback to drive galactic winds. In addition, alternative star formation prescriptions that aim to better capture small scale star formation physics will impact the effectiveness of feedback by altering the clustering properties of SNe (both in space and time). Finally, it is worth noting that there exists some minimum resolution requirement for the driving of outflows with individually time resolved SN because the injection of momentum (even if it is the physically correct amount) into too much mass will result in unphysically slow gas velocities.

Finally, it is worth pointing out that the resolution requirements for the mechanical feedback scheme to work well in terms of outflows is within the reach of next generation cosmological zoom-in simulations (at least for low mass systems). This will allow us to explore realistic SN feedback in a full cosmological environment, self-consistently taking into account the circulation of complex gas flows all the way from the cosmic web to the ISM. The adoption of a more accurate star formation prescription in concert with the inclusion of other forms of stellar feedback in such simulations may ultimately help us unveil what shapes star formation in low mass systems.

6 ACKNOWLEDGEMENTS

MCS is supported by the Science and Technology Facilities Council (STFC). DS and SS acknowledge support by the STFC and the ERC Starting Grant 638707 “Black holes and their host galaxies: co-evolution across cosmic time”. SS also acknowledges support from ERC Advanced Grant 320596 “The Emergence of Structure During the Epoch of Reionization”. This work was performed on the following: DiRAC Darwin Supercomputer hosted by the University of Cambridge High Performance Computing Service (<http://www.hpc.cam.ac.uk/>), provided by Dell Inc. using Strategic Research Infrastructure Funding from the Higher Education Funding Council for England and funding from the Science and Technology Facilities Council; DiRAC Complexity system, operated by the University of Leicester IT Services. This equipment is funded by BIS National E-Infrastructure capital grant ST/K000373/1 and STFC DiRAC Operations grant ST/K0003259/1; COSMA Data Centric system at Durham University, operated by the Institute for Computational Cosmology on behalf of the STFC DiRAC HPC Facility. This equipment was funded by a BIS National E-infrastructure capital grant ST/K00042X/1, STFC capital grant ST/K00087X/1, DiRAC Operations grant ST/K003267/1 and Durham University. DiRAC is part of the National E-Infrastructure.

REFERENCES

- Agertz O., Kravtsov A. V., 2015, *ApJ*, 804, 18
 Agertz O., Kravtsov A. V., Leitner S. N., Gnedin N. Y., 2013, *ApJ*, 770, 25
 Agertz O., Teyssier R., Moore B., 2011, *MNRAS*, 410, 1391
 Aguirre A., Hernquist L., Schaye J., Katz N., Weinberg D. H., Gardner J., 2001, *ApJ*, 561, 521
 Aumer M., White S. D. M., Naab T., Scannapieco C., 2013, *MNRAS*, 434, 3142
 Bauer A., Springel V., 2012, *MNRAS*, 423, 2558
 Behroozi P. S., Wechsler R. H., Conroy C., 2013, *ApJ*, 770, 57
 Bigiel F., Leroy A., Walter F., Brinks E., de Blok W. J. G., Madore B., Thornley M. D., 2008, *AJ*, 136, 2846
 Bland-Hawthorn J., Veilleux S., Cecil G., 2007, *Ap&SS*, 311, 87
 Blondin J. M., Wright E. B., Borkowski K. J., Reynolds S. P., 1998, *ApJ*, 500, 342
 Bolatto A. D. et al., 2013, *Nature*, Volume 499, Issue 7459, pp. 450-453 (2013), 499, 450
 Cen R., 1992, *ApJS*, 78, 341
 Ceverino D., Klypin A., 2009, *ApJ*, 695, 292
 Chevalier R. A., 1974, *ApJ*, 188, 501
 Christensen C. R., Davé R., Governato F., Pontzen A., Brooks A., Munshi F., Quinn T., Wadsley J., 2016, *ApJ*, 824, 57
 Cioffi D. F., McKee C. F., Bertschinger E., 1988, *ApJ*, 334, 252
 Conroy C., Kratter K. M., 2012, *ApJ*, 755, 123
 Dale J. E., Ngoumou J., Ercolano B., Bonnell I. A., 2014, *MNRAS*, 442, 694
 Dalla Vecchia C., Schaye J., 2008, *MNRAS*, 387, 1431
 Dalla Vecchia C., Schaye J., 2012, *MNRAS*, 426, 140
 Davé R., Katz N., Oppenheimer B. D., Kollmeier J. A., Weinberg D. H., 2013, *MNRAS*, 434, 2645
 Dubois Y., Teyssier R., 2008, *A&A*, 477, 79
 Dubois Y., Volonteri M., Silk J., Devriendt J., Slyz A., Teyssier R., 2015, *MNRAS*, 452, 1502
 Evans N. J., 1999, *ARA&A*, 37, 311
 Evans N. J. et al., 2009, *ApJS*, 181, 321
 Federrath C., Klessen R. S., 2012, *ApJ*, 761, 156
 Geen S., Rosdahl J., Blaizot J., Devriendt J., Slyz A., 2015, *MNRAS*, 448, 3248
 Genel S. et al., 2012, *ApJ*, 745, 11
 Governato F. et al., 2010, *Nature*, 463, 203
 Haid S., Walch S., Naab T., Seifried D., Mackey J., Gatto A., 2016, *MNRAS*, 460, 2962
 Hennebelle P., Chabrier G., 2011, *ApJ*, 743, L29
 Hopkins P. F., Kereš D., Oñorbe J., Faucher-Giguère C.-A., Quataert E., Murray N., Bullock J. S., 2014, *MNRAS*, 445, 581
 Hopkins P. F., Narayanan D., Murray N., 2013, *MNRAS*, 432, 2647
 Hopkins P. F., Quataert E., Murray N., 2011, *MNRAS*, 417, 950
 Hopkins P. F., Quataert E., Murray N., 2012a, *MNRAS*, 421, 3522
 Hopkins P. F., Quataert E., Murray N., 2012b, *MNRAS*, 421, 3488
 Hopkins P. F. et al., 2017, *arXiv:1702.06148*
 Hopkins P. F. et al., 2018, *MNRAS*, sty674
 Hu C.-Y., Naab T., Glover S. C. O., Walch S., Clark P. C., 2017, *MNRAS*, 471, 2151
 Hu C.-Y., Naab T., Walch S., Glover S. C. O., Clark P. C., 2016, *MNRAS*, 458, 3528
 Iffrig O., Hennebelle P., 2015, *A&A*, 576, A95
 Katz N., Weinberg D. H., Hernquist L., 1996, *ApJS*, 105, 19
 Kennicutt R. C., 1998, *ApJ*, 498, 541
 Kennicutt, Robert C. J., 1989, *ApJ*, 344, 685
 Kereš D., Katz N., Davé R., Fardal M., Weinberg D. H., 2009, *MNRAS*, 396, 2332
 Kereš D., Vogelsberger M., Sijacki D., Springel V., Hernquist L., 2012, *MNRAS*, 425, 2027
 Kim C.-G., Ostriker E. C., 2015, *ApJ*, 802, 99
 Kim C.-G., Ostriker E. C., 2016, *arXiv:1612.03918*
 Kimm T., Cen R., 2014, *ApJ*, 788, 121
 Kimm T., Cen R., Devriendt J., Dubois Y., Slyz A., 2015, *MNRAS*, 451, 2900
 Kimm T., Katz H., Haehnelt M., Rosdahl J., Devriendt J., Slyz A., 2017, *MNRAS*, 466, 4826
 Kroupa P., 2002, *Science*, 295, 82
 Krumholz M. R., McKee C. F., 2005, *ApJ*, 630, 250
 Krumholz M. R., Tan J. C., 2007, *ApJ*, 654, 304
 Leitherer C. et al., 1999, *ApJS*, 123, 3
 Li J. T., 2015, *MNRAS*, 453, 1062
 Martin C. L., 1999, *ApJ*, 513, 156
 Martin C. L., Kennicutt, Jr. R. C., 2001, *ApJ*, 555, 301
 Martin C. L., Scannapieco E., Ellison S. L., Hennawi J. F., Djorgovski S. G., Fournier A. P., 2010, *ApJ*, 721, 174
 Martin C. L., Shapley A. E., Coil A. L., Kornei K. A., Bundy K., Weiner B. J., Noeske K. G., Schiminovich D., 2012, *ApJ*, 760, 127
 Martizzi D., Faucher-Giguère C.-A., Quataert E., 2015, *MNRAS*, 450, 504
 Martizzi D., Fielding D., Faucher-Giguère C. A., Quataert E., 2016, *MNRAS*, 459, 2311

Mitra S., Davé R., Finlator K., 2015, *MNRAS*, 452, 1184
 Moster B. P., Naab T., White S. D. M., 2013, *MNRAS*, 428, 3121
 Murray N., Quataert E., Thompson T. A., 2010, *ApJ*, 709, 191
 Navarro J., Frenk C. S., White S. D. M., 1997, *ApJ*, 490, 493
 Oppenheimer B. D., Davé R., 2006, *MNRAS*, 373, 1265
 Ostriker J. P., McKee C. F., 1988, *Rev. Mod Phys.*, 60, 1
 Padoan P., Nordlund A. k., 2011, *ApJ*, 730, 40
 Pettini M., Madau P., Bolte M., Prochaska J. X., Ellison S. L., Fan X., 2003, *ApJ*, 594, 695
 Pettini M., Shapley A. E., Steidel C. C., Cuby J.-G., Dickinson M., Moorwood A. F. M., Adelberger K. L., Gialalisco M., 2001, *ApJ*, 554, 981
 Puchwein E., Springel V., 2013, *MNRAS*, 428, 2966
 Rosdahl J., Schaye J., Dubois Y., Kimm T., Teyssier R., 2017, *MNRAS*, 466, 11
 Rosdahl J., Schaye J., Teyssier R., Agertz O., 2015, *MNRAS*, 451, 34
 Roškar R., Teyssier R., Agertz O., Wetzstein M., Moore B., 2014, *MNRAS*, 444, 2837
 Sales L. V., Marinacci F., Springel V., Petkova M., 2014, *MNRAS*, 439, 2990
 Sales L. V., Navarro J. F., Schaye J., Vecchia C. D., Springel V., Booth C. M., 2010, *MNRAS*, 409, 1541
 Schroetter I., Bouché N., Péroux C., Murphy M. T., Continini T., Finley H., 2015, *ApJ*, 804
 Sedov L. I., 1959, *Similarity and Dimensional Methods in Mechanics*. Academic Press, New York
 Shen S., Madau P., Aguirre A., Guedes J., Mayer L., Wadsley J., 2012, *ApJ*, 760, 50
 Sijacki D., Vogelsberger M., Kereš D., Springel V., Hernquist L., 2012, *MNRAS*, 424, 2999
 Songaila A., 2005, *AJ*, 130, 1996
 Songaila A., 2006, *AJ*, 131, 24
 Soto K. T., Martin C. L., Prescott M. K. M., Armus L., 2012, *ApJ*, 757
 Springel V., 2010, *MNRAS*, 401, 791
 Springel V., Di Matteo T., Hernquist L., 2005, *MNRAS*, 361, 776
 Springel V., Hernquist L., 2003, *MNRAS*, 339, 289
 Stinson G., Seth A., Katz N., Wadsley J., Governato F., Quinn T., 2006, *MNRAS*, 373, 1074
 Strickland D. K., Heckman T. M., 2007, *ApJ*, 658, 258
 Strickland D. K., Heckman T. M., 2009, *ApJ*, 697, 2030
 Taylor G., 1950, *Proc. R. Soc. A*, 201, 175
 Teyssier R., Chapon D., Bournaud F., 2010, *ApJ*, 720, L149
 Teyssier R., Pontzen A., Dubois Y., Read J. I., 2013, *MNRAS*, 429, 3068
 Thornton K., Gaudlitz M., Janka H., Steinmetz M., 1998, *ApJ*, 500, 95
 Torrey P., Vogelsberger M., Sijacki D., Springel V., Hernquist L., 2012, *MNRAS*, 427, 2224
 Truelove J. K., Klein R. I., McKee C. F., Holliman Ii J. H., Howell L. H., Greenough J. A., 1997, *ApJ*, 489, 179
 Vázquez-Semadeni E., Colín P., Gómez G. C., Ballesteros-Paredes J., Watson A. W., 2010, *ApJ*, 715, 1302
 Veilleux S., Cecil G., Bland-Hawthorn J., 2005, *ARA&A*, 43, 769
 Vogelsberger M., Genel S., Sijacki D., Torrey P., Springel V., Hernquist L., 2013, *MNRAS*, 436, 3031

Vogelsberger M., Sijacki D., Keres D., Springel V., Hernquist L., 2012, *MNRAS*, 425, 3024
 Walch S., Naab T., 2015, *MNRAS*, 451, 2757
 Walch S. K., Whitworth A. P., Bisbas T., Wünsch R., Hubber D., 2012, *MNRAS*, 427, 625
 Walter F. et al., 2017, *ApJ*, 835, 265
 Walter F., Weiss A., Scoville N., 2002, *ApJ*, 580, L21
 White S. D. M., Frenk C. S., 1991, *ApJ*, 379, 52
 Williams J. P., McKee C. F., 1997, *ApJ*, 476, 166
 Woltjer L., 1972, *ARA&A*, 10, 129
 Wyder T. K. et al., 2009, *ApJ*, 696, 1834
 Zuckerman B., Evans N. J., 1974, *ApJl*, 192, L149

APPENDIX A: NON-THERMAL PRESSURE FLOOR

As described in Section 2.2 we impose a non-thermal pressure floor to avoid artificial fragmentation that may occur when the Jeans length is not properly resolved. Setting a minimum pressure using equation (1) ensures that the resulting Jeans length is always resolved by at least N_J cells. Truelove et al. (1997) suggests that, at a minimum, the Jeans length must be resolved by at least 4 cells. This criteria is widely adopted in gravitational hydrodynamic simulations, but a variety of values can be found in the literature. The choice of N_J is non-trivial: too low and artificial fragmentation will occur, too high and the formation of small (physical) structures that would otherwise be resolved is suppressed. Fig. A1 shows the effect of various choices of N_J on the morphology of our fiducial galaxy model at 100 Myr with no feedback with 1000 M_\odot resolution. It can be seen that with no pressure floor ($N_J = 0$) the disk fragments into multiple, small, high density clumps. At the other extreme, enforcing resolution of the Jeans length by 16 cells ($N_J = 16$) results in the washing out of all small structure save some weakly defined spiral arms. Other choices of N_J in between these values results in a corresponding sliding scale of morphologies. We can reasonably confidently assume that the adoption of $N_J = 16$ results in a morphology that is over-smoothed. Unfortunately, it is not so easy to say what the correct lower limit of N_J is. Determining exactly when the onset of artificial fragmentation occurs is a non-trivial problem that is beyond the scope of this work.

We attempt to crudely quantify the degree of fragmentation in Fig. A2 by plotting the mass of gas above some density and the mass of newly formed stars for our various choices of N_J . Mass of gas above 100 cm^{-3} decreases by well over an order of magnitude across the range of N_J probed, with even more dramatic increases when examining higher densities and, perhaps more worryingly, mass in new stars. It can be seen that a definite transition occurs from a regime of suppression of high density gas to a regime where gas may reach these densities, though this transition happens at different values of N_J depending on the density examined. For example, for densities above 100 cm^{-3} the transition occurs at $N_J \sim 10$, while for densities above 10^3 cm^{-3} and 10^4 cm^{-3} the transitions occurs at $N_J \sim 8$ and ~ 6 , respectively. This transition could represent the transition between an artificially fragmenting regime to a stabilised regime, but without a more careful determination of what ‘artificial fragmentation’ is, one could just as easily state that it merely marks the transition from over-smoothing of

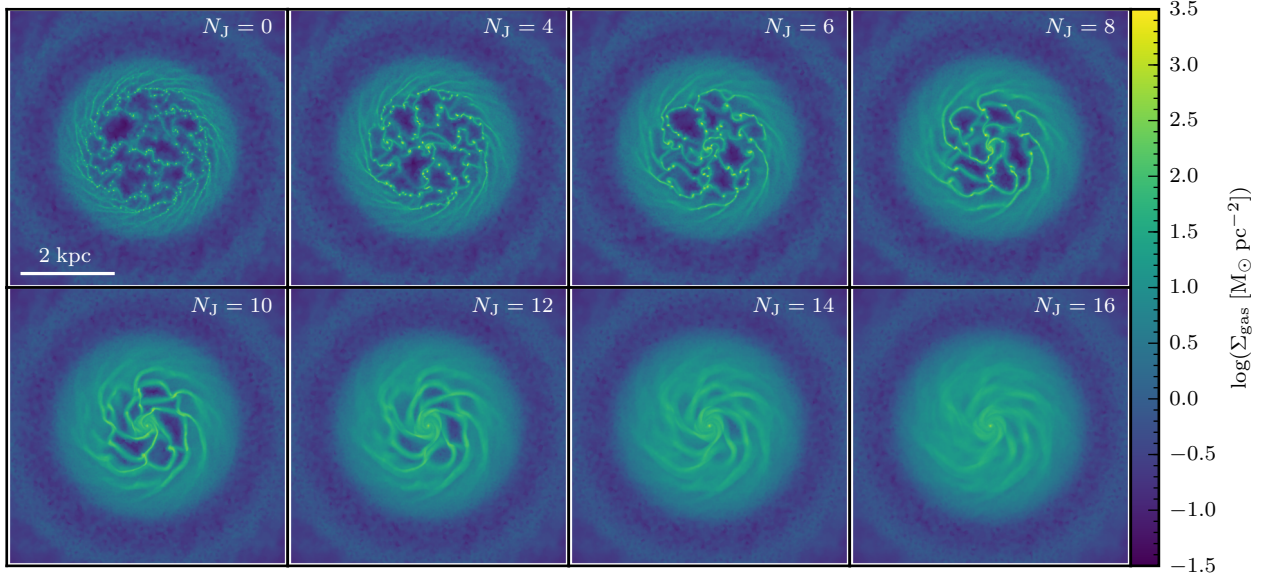


Figure A1. Face-on gas density projections of simulations after 100 Myr with varying values of N_J used to determine the artificial pressure floor, where N_J is the number of cells by which the Jeans length must be resolved. Each simulation is carried out with no feedback and at $1000 M_\odot$ resolution using our fiducial galaxy model. While imposing no floor results in artificial fragmentation on the smallest scales (top left panel), the $N_J = 16$ run (bottom right) washes out the physical structures present in the disk.

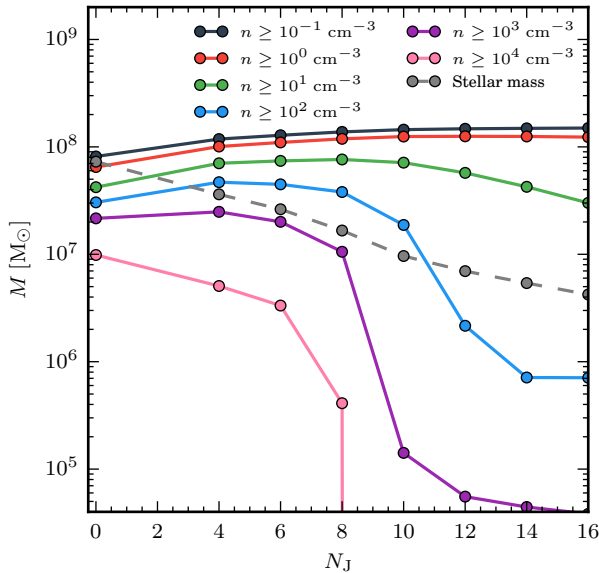


Figure A2. The mass above a given density (or stellar mass, grey dashed curve) as function of N_J at 100 Myr. Each value is measured from a simulation with no feedback at $1000 M_\odot$ resolution using our fiducial galaxy model. Note that there is a clear suppression of gas mass above a given density for densities above 100 cm^{-3} which motivates our choice of the reasonable N_J value to adopt, but for the stellar mass no such trend exists.

structure to a properly resolved regime. Hence, the choice of N_J becomes somewhat arbitrary, which is certainly not ideal given the impact the choice has on the subsequent evolution of the galaxy. With this in mind, we choose a fiducial

value of $N_J = 8$ for $1000 M_\odot$ resolution simulations. This lies between the two extremes of small scale fragmentation and total suppression of high density gas. It also produces a galaxy morphology similar to that found in other works containing simulations of a similar type that use pressure floors (e.g. Rosdahl et al. 2015, 2017) though it should be noted that these works adopt different values of N_J from us and from each other. This is not a particularly satisfactory way of choosing the strength of the pressure floor but it is necessary to allow the comparison of our feedback models with those in other works.

If one assumes that there is a single ‘correct’ value of N_J that should be used to avoid artificial fragmentation, then it follows that this value is resolution independent. In other words, there exists some minimum required number of cells to correctly resolve fragmentation. Using a fixed value of N_J then allows fragmentation to occur on smaller scales as the minimum resolvable length decreases as resolution is increased. While this is often a desirable behaviour, particularly when concerned with ISM properties on the edge of the resolution limit, it necessarily leads to divergent galaxy properties. Instead, scaling N_J such that the minimum resolved Jeans length corresponds to the same physical scale at all resolutions results in convergent morphologies. In Fig. A3, we compare the $1000 M_\odot$ resolution simulation with $N_J = 8$ (as in Fig. A1) with two simulations with a resolution of $100 M_\odot$. One uses a value of $N_J = 8$, the other uses a value of $N_J = 17.2$ (i.e. scaled with mass resolution such that the minimum Jeans length is the same at both resolutions). It is clear that using the same value of N_J results in very different morphologies, whereas the adoption of a higher value with better resolution results in a similar morphology. This is not to say that the $1000 M_\odot$ resolution, $N_J = 8$ and $100 M_\odot$ resolution, $N_J = 17.2$ results are

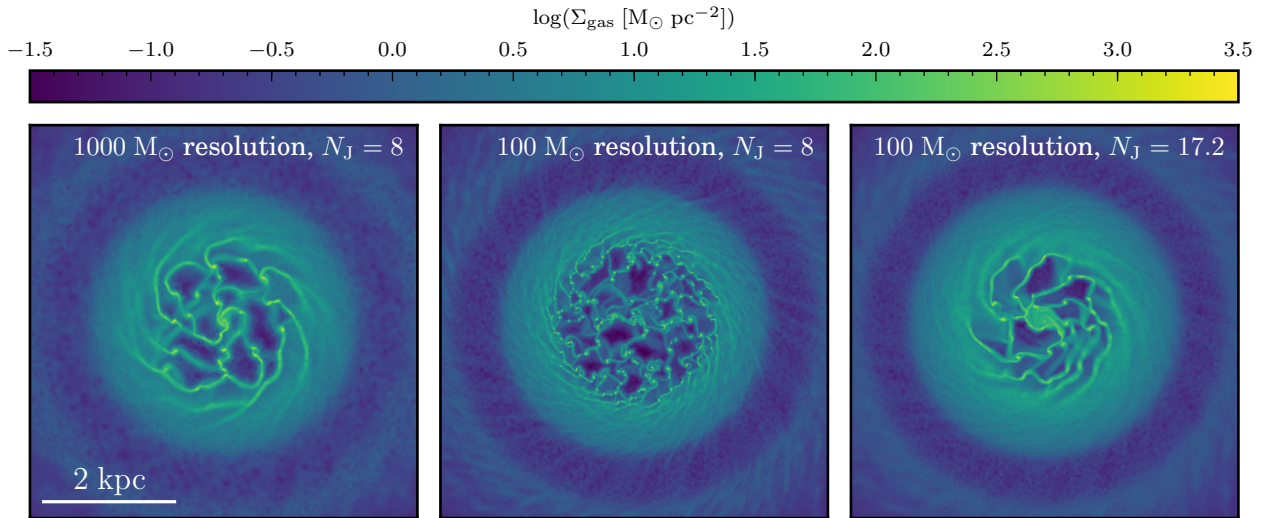


Figure A3. Face-on gas density projections after 100 Myr comparing our fiducial choice of $N_J = 8$ for a $1000 M_\odot$ resolution simulation with the same value for a $100 M_\odot$ resolution simulation (i.e. assuming that the ‘correct’ choice for N_J is resolution independent) and $N_J = 17.2$ (i.e. such that the Jeans length is resolved by the same physical scale between resolutions). Each simulation is with no feedback using our fiducial galaxy model.

more ‘correct’ than the other, since as previously mentioned, it is difficult to determine when artificial fragmentation occurs. However, for the purposes of this paper where we are primarily concerned about the effects of differing SNe feedback implementations, particularly *examining the role of the resolution adopted on the feedback*, we find that it is advantageous to enforce approximately similar galaxy evolutions in the no feedback case across our resolutions by scaling the value of N_J with resolution as described in Section 2.2. This we broadly achieve, with the no feedback simulations at different resolutions producing same amount of stars within a factor of a few and having comparable morphologies (see Figs. 1, D1 and D2). It is worth highlighting that we are not unique in our choice to scale N_J with resolution (see for example Rosdahl et al. 2015, 2017).

When we try to run simulations without a pressure floor but with feedback, the effect is similar to increasing the star formation efficiency parameter (see Fig. 13), with a sudden burst of high SFR followed by extremely strong feedback that largely destroys the disk and quenches star formation. It is possible that if we included other stellar feedback mechanisms (stellar winds, radiation pressure, photoionisation) that are active in the intervening time between star formation and SN occurrence it might be possible to keep gas from entering the regime where it is vulnerable to artificial fragmentation, thus removing the need for a pressure floor. Alternatively, a more complex star formation criteria that identifies fragmenting gas could also circumvent the issue (e.g. Hopkins et al. (2017) argue that the Jeans unstable gas should be turned into stars rather than using a pressure floor), but if the Jeans length is significantly under-resolved this could result in the spurious boosting of SFRs. We conclude this section by remarking that, on the whole, when artificial pressure floors are adopted, the motivation behind the choice of parameters is often not clear. Given the strong dependence of results on this choice, we suggest that this is

an issue that needs to be addressed in more detail in future work.

APPENDIX B: SPH-LIKE KERNEL WEIGHTING VS. EXPLICITLY ISOTROPIC WEIGHTING SCHEME FOR SNE FEEDBACK

As mentioned in Section 2.4, we have found that under certain conditions, the use of a simple SPH-like kernel-based weighting scheme for distributing feedback quantities (mass, metals, energy and momentum) into the gas local to the SNe can result in significant violations of the desired isotropic distribution. Because such a weighting scheme preferentially injects into denser regions where there are more cells, if there is a strong density gradient in a particular direction injection of feedback quantities will be injected perpendicular to the gradient. For example, in the case of a SN occurring in a thin disk, more resolution elements lie in the disk plane than lie above and below it so feedback quantities will be preferentially injected into the disk plane. The situation is exacerbated by poor resolution and by the use of efficient momentum-based feedback schemes (thermal injection based schemes can mitigate the situation slightly since heated cells will tend to expand along the path of least resistance). This can result in the unphysical driving of expanding shells through the disk plane, with little ejecta going in the vertical direction (see also Hopkins et al. 2017; Hopkins et al. 2018).

Fig. B1 demonstrates this effect. We compare a simulation using a standard SPH-kernel based mass weighting scheme for distributing feedback quantities with our explicitly isotropic weighting scheme as described in Section 2.4. For numerical reasons, we cannot use our full mechanical feedback scheme with an SPH-like scheme, so we use a hybrid of our kinetic and mechanical feedback schemes for this comparison; we inject $2.41 \times 10^5 \text{ km s}^{-1} M_\odot$ of momentum per SNe, corresponding to the final momentum of a SN occurring in gas of density 100 cm^{-3} and metallicity $0.1 Z_\odot$ as

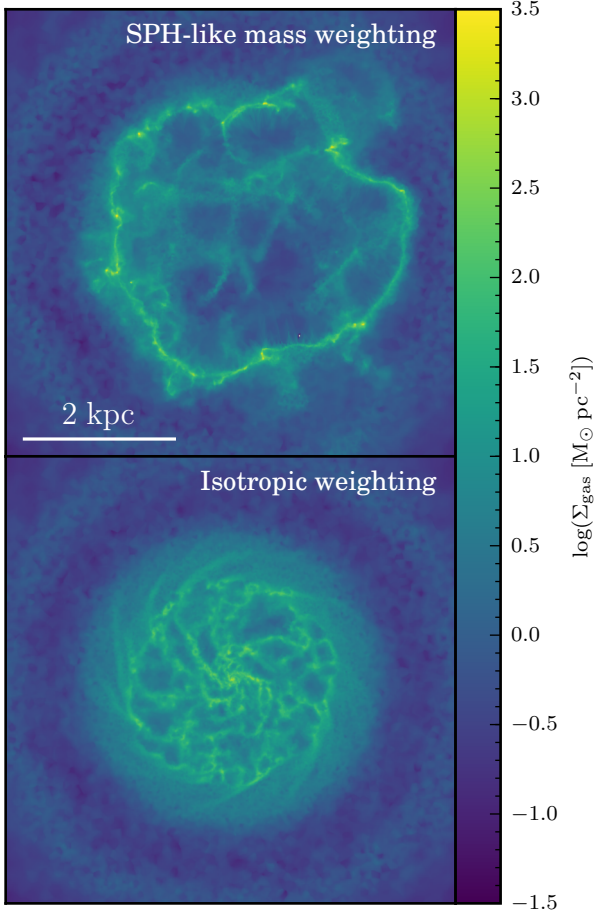


Figure B1. Face-on gas density projections of simulations at 100 Myr comparing the use of an SPH-like mass weighting scheme for distributing SNe mass, energy and momentum with our explicitly isotropic weighting scheme described in Section 2.4. The simulations have a resolution of $2000 M_{\odot}$, use our fiducial galaxy model with a modified form of our mechanical feedback (see main text). SPH-like weighting leads to unphysical shells propagating through the disk, sweeping up most of its mass. Our isotropic weighting scheme avoids this numerical issue correctly coupling the SN ejecta to the surrounding gas regardless of its density.

calculated using equation (22). The simulations are of our fiducial galaxy at $2000 M_{\odot}$ resolution and the projections shown in Fig. B1 are at 100 Myr. The SPH-like weighting scheme sweeps the disk mass into a thin expanding ring, whereas our isotropic scheme prevents this occurring. This scenario is where the effect is most noticeable, but it is still present to some extent at higher resolutions.

It should be noticed that switching to a volume weighting scheme rather than mass weighting does not have much of an effect. For a reasonable neighbour number (32 - 64, as used with a cubic spline kernel) most identified neighbours will be in the disk plane. If cells are found within the smoothing length containing the neighbours that lie above the plane of the disk, the extra weighting they will receive for being of a larger volume (because they are less dense) is likely to be subdominant compared to the ‘penalty’ they receive for being furthest away from the star particle.

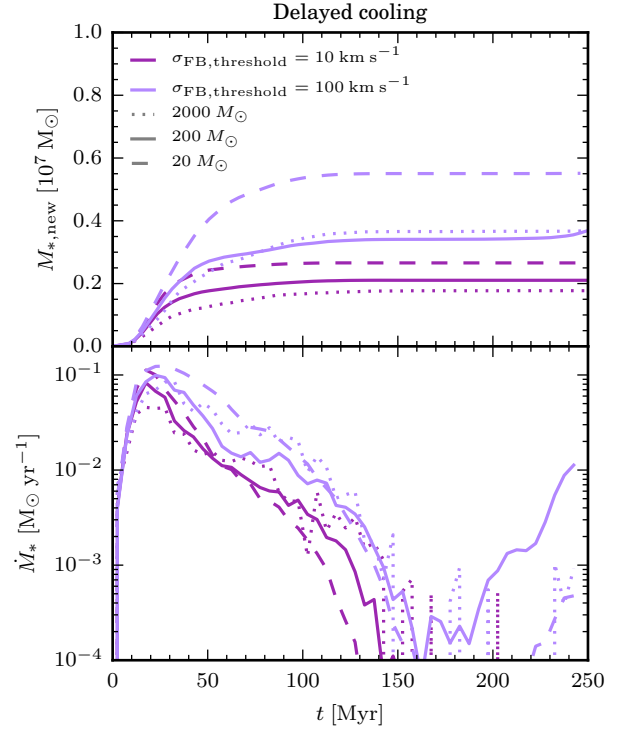


Figure C1. Newly formed stellar mass (top) and SFRs (bottom) for simulations at all three resolutions for runs with delayed cooling using our fiducial threshold of 10 km s^{-1} and a higher value of 100 km s^{-1} . The results are not very sensitive to the change of $\sigma_{\text{FB,threshold}}$ and while the SFRs are suppressed somewhat less with the choice of the higher value, the disk is still largely disrupted after the first peak in SFR.

APPENDIX C: OTHER DELAYED COOLING PARAMETERS

As our fiducial parameters for the delayed cooling with fixed dissipation time we have adopted $t_{\text{diss}} = 10 \text{ Myr}$ and $\sigma_{\text{FB}} = 10 \text{ km s}^{-1}$, as used in Teyssier et al. (2013). As noted above, with our galaxy models at all resolutions explored, this feedback scheme appears to be very strong relative to our other schemes and produces unphysical results. We therefore tried a higher threshold velocity dispersion, $\sigma_{\text{FB,threshold}} = 100 \text{ km s}^{-1}$, as used in Rosdahl et al. (2017). Fig. C1 shows the effect of using these parameters on the star formation rate and stellar masses with our fiducial galaxy model at all three of our resolutions. The SFRs are not suppressed to the same degree with this weaker feedback, with final new stellar mass being approximately a factor of 2 larger at all resolutions. However, the feedback still destroys the disk in the same manner as our fiducial simulations (though gas returns to the centre, resulting in a second burst of star formation). As mentioned above, with a more careful approach to tuning these parameters, we could perhaps arrive at a less aggressive scheme.

APPENDIX D: OTHER RESOLUTIONS

This appendix contains results for our lower resolution simulations for comparison to the figures in the main text that show our highest resolution simulations. Figs. D1 and D2 show face-on and edge-on density projections of gas and

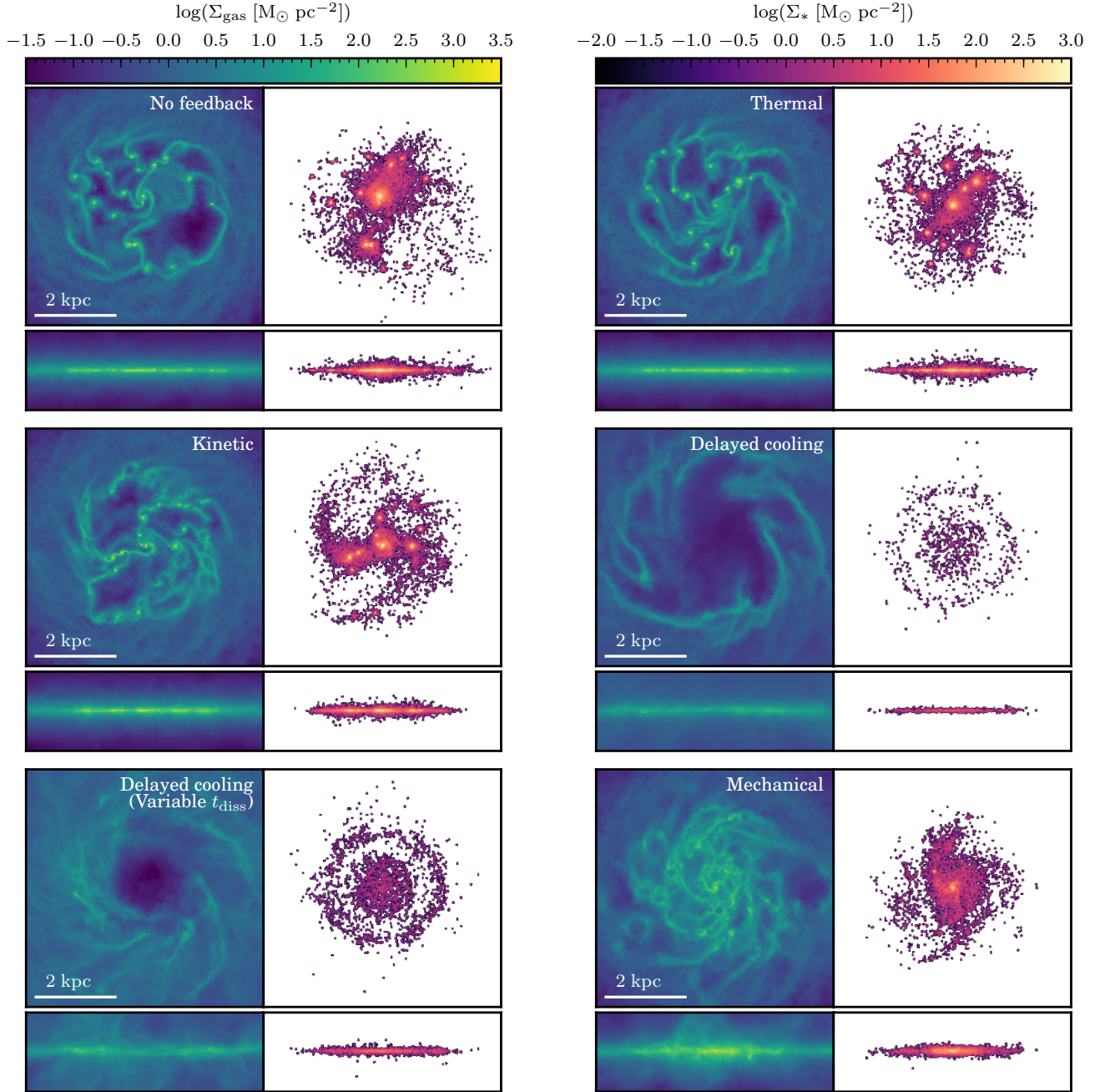


Figure D1. Projections of gas and new stars formed for our different feedback simulation at 250 Myr for $2000 M_{\odot}$ resolution runs. The mixed feedback simulation is not shown as the results are similar to the thermal and kinetic feedback simulations. The morphology of the no feedback simulation disk is similar to the highest resolution case (see Fig. 1), with a highly clumpy distribution of gas and newly formed stars, although the structure is less well defined at this resolution (particularly in the stellar component). At this resolution, the classical feedback schemes overcool, so they produce similar morphologies to the no feedback simulation. Both delayed feedback schemes are too powerful, disrupting the gas disk and producing ring-like structures of newly formed stars. The mechanical feedback scheme is able to suppress the formation of dense clumps without destroying the disk. The resulting morphology is similar to the high resolution simulation, although it is not as well defined.

newly formed stars after 250 Myr (see Fig. 1 for the highest resolution case). Fig. D3 shows density, temperature and metallicity slices at 250 Myr to demonstrate how outflow properties change with resolution (see Fig. 7 for the highest resolution case).

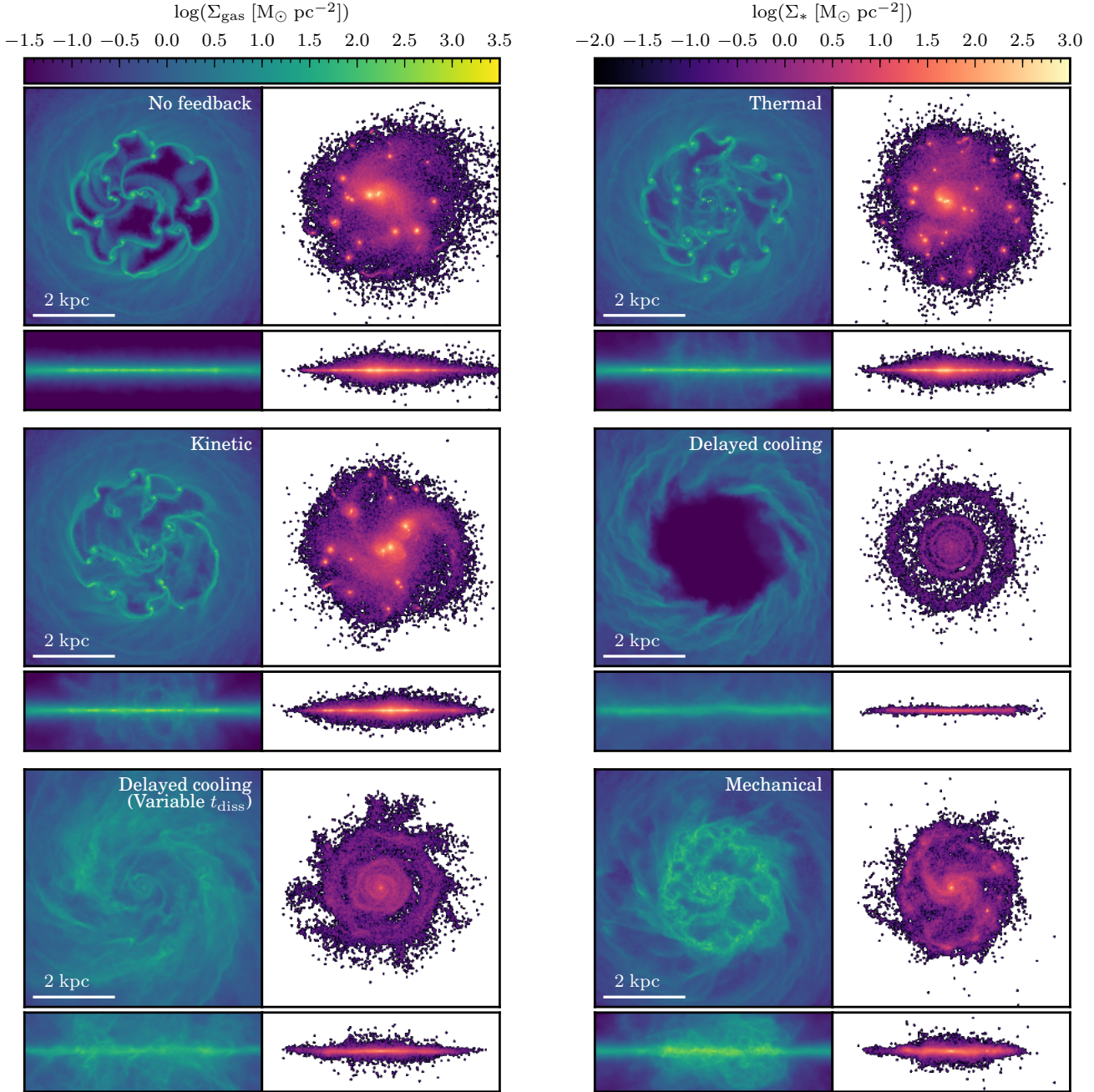


Figure D2. Projections of gas and new stars formed for our different feedback simulation at 250 Myr for $200 M_{\odot}$ resolution runs. The mixed feedback simulation is not shown as the results are similar to the thermal and kinetic feedback simulations. The morphology of the no feedback simulation disk is similar to the highest and lowest resolution cases (see Figs. 1 and D1). As in the lowest resolution simulation, the classical feedback schemes overcool and produce a similar clumped morphology to the no feedback simulation. The delayed feedback schemes remain too powerful, disrupting the gas disk, although the scheme with variable t_{diss} is weaker. The mechanical feedback scheme produces a similar morphology to the lower and higher resolutions simulations.

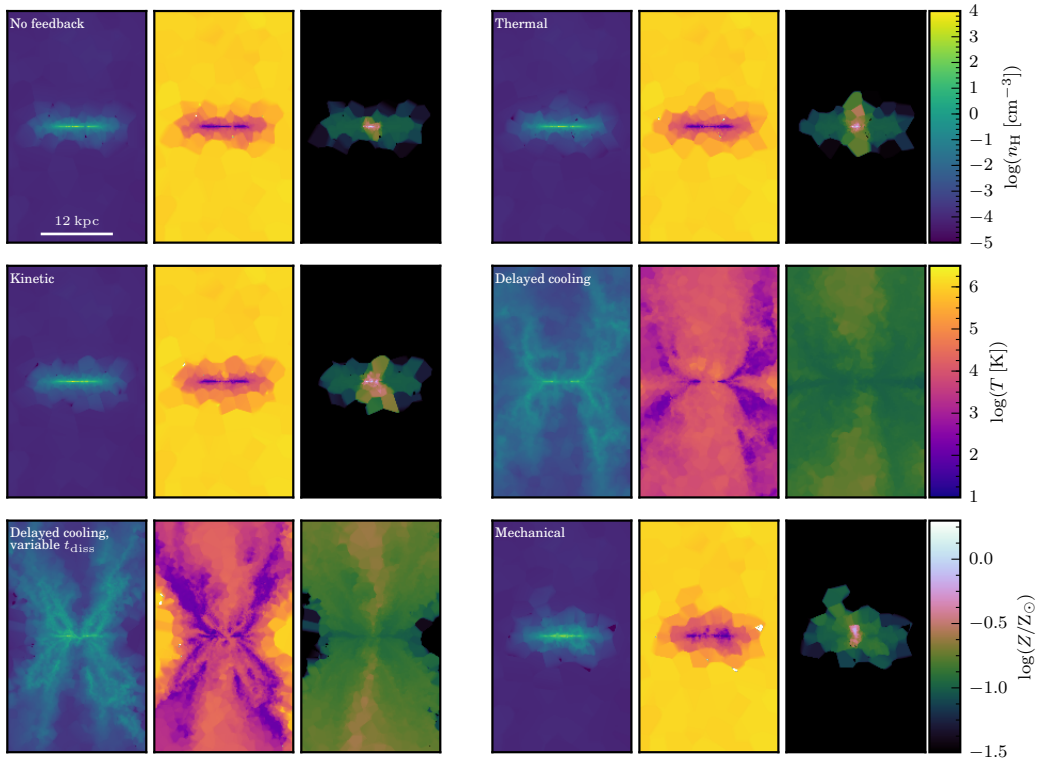
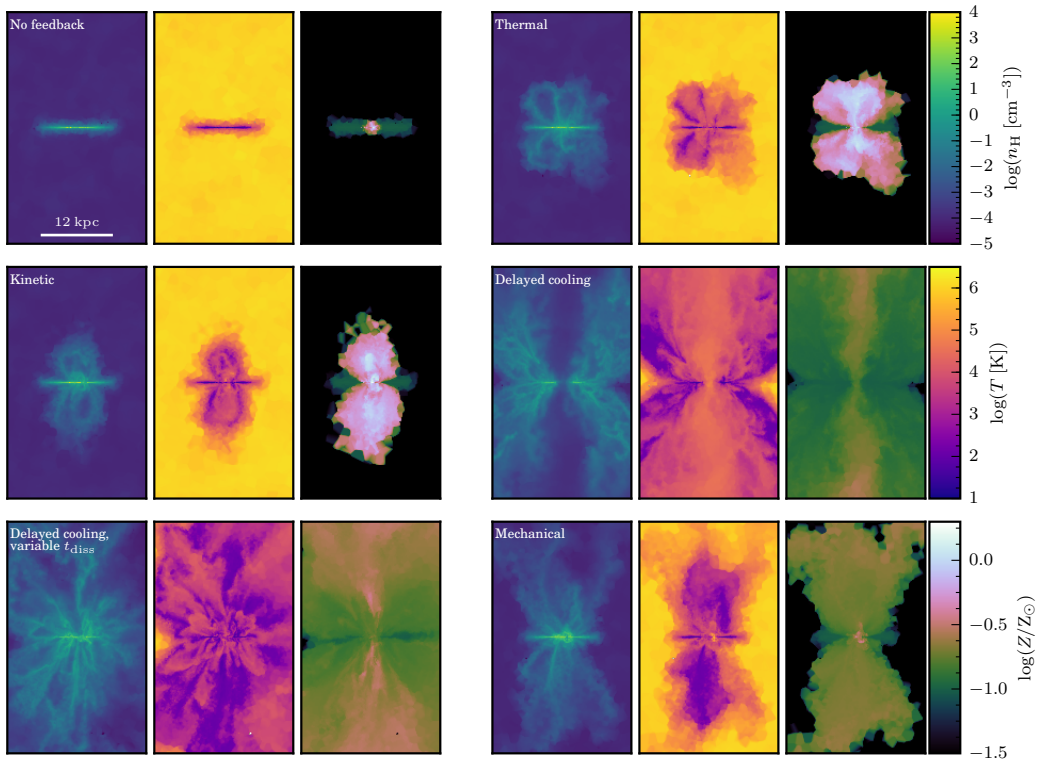
2000 M_{\odot} resolution200 M_{\odot} resolution

Figure D3. Density, temperature and metallicity slices at 250 Myr for 2000 and 200 M_{\odot} resolution runs (top and bottom respectively). The mixed feedback simulation is not shown as the results are similar to the thermal and kinetic feedback simulations. Unsurprisingly, the no feedback simulations do not produce outflows. Only the delayed cooling schemes drive outflows at both resolutions, ejecting the majority of material from the centre of the system. At the 200 M_{\odot} resolution, the classical feedback schemes produce outflows that reach a short distance above the disk. They are highly metal enriched because of the large number of SNe driving the outflows, due to the inefficiency of the feedback caused by overcooling. The mechanical feedback is able to drive a modest outflow at the 200 M_{\odot} resolution, though the outflow peaked ~ 100 Myr previously resulting in material returning to the disk in a galactic fountain (see Figs. 5 and 6).